Inorg. Chem. **2003**, *42*, 7001–7017

Inorganic Chemistry
Article

A New Family of Spin Crossover Complexes with a Tripod Ligand Containing Three Imidazoles: Synthesis, Characterization, and Magnetic Properties of $[Fe^{II}H_3L^{Me}](NO_3)_2\cdot1.5H_2O$, $[Fe^{III}L^{Me}]\cdot3.5H_2O$, $[Fe^{II}H_3L^{Me}][Fe^{II}L^{Me}]NO_3$, and $[Fe^{II}H_3L^{Me}][Fe^{III}L^{Me}](NO_3)_2$ (H_3L^{Me} = Tris[2-(((2-methylimidazol-4-yl)methylidene)amino)ethyl]amine)

Yuichi Ikuta,[†] Makoto Ooidemizu,[†] Yuichi Yamahata,[†] Masahiro Yamada,[†] Shutaro Osa,[†] Naohide Matsumoto,[*,†] Seiichiro Iijima,[‡] Yukinari Sunatsuki,[§] Masaaki Kojima,[§] Françoise Dahan,[||] and Jean-Pierre Tuchagues[||]

Department of Chemistry, Faculty of Science, Kumamoto University, Kurokami 2-39-1,
Kumamoto 860-8555, Japan, National Institute of Advanced Industrial Science and Technology,
Tsukuba 305-8566, Japan, Department of Chemistry, Faculty of Science, Okayama University,
Tsushima-naka 3-1-1, Okayama 700-8530, Japan, and Laboratoire de Chimie de Coordination du
CNRS, UP 8241, 205 Route de Narbonne, 31077 Toulouse Cedex, France

Received May 10, 2003

A new family of spin crossover complexes, $[Fe^{II}H_3L^{Me}](NO_3)_2\cdot1.5H_2O$ (**1**), $[Fe^{III}L^{Me}]\cdot3.5H_2O$ (**2**), $[Fe^{II}H_3L^{Me}][Fe^{II}L^{Me}]NO_3$ (**3**), and $[Fe^{II}H_3L^{Me}][Fe^{III}L^{Me}](NO_3)_2$ (**4**), has been synthesized and characterized, where H_3L^{Me} denotes a hexadentate N_6 tripod ligand containing three imidazole groups, tris[2-(((2-methylimidazol-4-yl)methylidene)amino)ethyl]amine. It was found that the spin and oxidation states of the iron complexes with this tripod ligand are tuned by the degree of deprotonation of the imidazole groups and by the 2-methyl imidazole substituent. Magnetic susceptibility and Mössbauer studies revealed that **1** is an HS-Fe^{II} complex, **2** exhibits a spin equilibrium between HS and LS-Fe^{III}, **3** exhibits a two-step spin transition, where the component $[Fe^{II}L^{Me}]^-$ with the deprotonated ligand participates in the spin transition process in the higher temperature range and the component $[Fe^{II}H_3L^{Me}]^{2+}$ with the neutral ligand participates in the spin transition process in the lower temperature range, and **4** exhibits spin transition of both the Fe^{II} and Fe^{III} sites. The crystal structure of **3** consists of homochiral extended 2D puckered sheets, in which the capped tripodlike components $[Fe^{II}H_3L^{Me}]^{2+}$ and $[Fe^{II}L^{Me}]^-$ are alternately arrayed in an up-and-down mode and are linked by the imidazole–imidazolate hydrogen bonds. Furthermore, the adjacent 2D homochiral sheets are stacked in the crystal lattice yielding a conglomerate as confirmed by the enantiomeric circular dichorism spectra. Compounds **3** and **4** showed the LIESST (light induced excited spin state trapping) and reverse-LIESST effects upon irradiation with green and red light, respectively.

Introduction

The field of metal-complex-based magnetic materials has shown spectacular advances in the past two decades.[1,2] In the latest decade, special attention has been devoted to multifunctional magnetic materials such as light-induced magnets,[3] electrically conductive magnets,[4] guest-absorbed magnetic switches,[5] etc., in which the different magnetic and electronic properties can be switched or interconverted by

---

[*] To whom correspondence should be addressed. E-mail: naohide@aster.sci.kumamoto-u.ac.jp. Fax: +81-96-342-3390.

[†] Kumamoto University.

[‡] National Institute of Advanced Industrial Science and Technology.

[§] Okayama University.

[||] Laboratoire de Chimie de Coordination du CNRS Toulouse.

(1) (a) Kahn, O. *Molecular Magnetism*; VCH: Weinheim, 1993. (b) *Magnetic Molecular Materials*; Gatteschi, D., Kahn, O., Miller, J. S., Palacio, F., Eds.; NATO ASI Series E; Kluwer Academic Publishers: Dordrecht, 1991; Vol. 198. (c) *Magnetism: A Supramolecular Function*; Kahn, O., Ed.; NATO ASI Series C; Kluwer Academic Publishers: Dordrecht, 1996; Vol. 484.

(2) (a) Miller, J. S.; Calabrese, J. C.; Rommelmann, H.; Chittipeddi, S. R.; Zhang, J. H.; Reiff, W. M.; Epstein, A. J. *J. Am. Chem. Soc.* **1987**, *109*, 769−781. (b) Kahn, O.; Pei, Y.; Verdaguer, M.; Renard, J. P.; Sletten, J. *J. Am. Chem. Soc.* **1988**, *110*, 782−789. (c) Tamaki, H.; Zhong, Z.; Matsumoto, N.; Kida, S.; Koikawa, M.; Achiwa, N.; Hashimoto, Y.; Okawa, H. *J. Am. Chem. Soc.* **1992**, *114*, 6974−6979.

10.1021/ic034495f CCC: $25.00

different physical perturbations. Now, a metal-complex-based magnet exhibiting a particular physical property can be rationally synthesized from programmed component molecules by a bottom-up method, in which the molecules designed are assembled into a multidimensional structure leading to a functional compound.[6] Since magnetic characteristics of ferromagnets or ferrimagnets, such as spontaneous magnetization and hysteresis, result from magnetic ordering of the constituting paramagnetic centers, the answer to the questions (i) how to control the magnetic interaction between nearest neighbors and (ii) how to extend the alignment of the magnetic vectors over the whole lattice should allow the molecular design of such magnets.

On the other hand, bistable molecules can be used as molecular switches in electronic devices through different external perturbations, where in principle a single molecule plays the role of a switching device. The bistability of organic bistable molecules such as diarylethenes, stilbene, and diazonium is brought on by a structural change (isomerization).[7] Inorganic bistable molecules based on coordination compounds possess two different stable electronic states, and hence, the different optical, magnetic, and electronic properties associated with the two electronic states can be switched by external physical perturbations. Therefore, inorganic bistable molecules have advantages over their organic counterparts due to their versatility in electronic structures and the possibility of addressing them with different physical perturbations. Spin-crossover compounds are the most spectacular and representative examples of molecular bistability.[8] Spin-crossover (SCO) between the low-spin (LS) and high-spin (HS) states is observed in some octahedral $3d^n$ ($4 \leq n \leq 7$) metal complexes and is induced by an external perturbation, such as temperature, pressure, or light irradiation. The SCO bistability can be one of the most promising new electronic devices in molecular memories and switches as it may be controlled by different physical perturbations. Since the discovery of the LIESST (light induced excited spin state trapping) and reverse-LIESST effects,[9] photoswitchable SCO compounds with long-lived metastable states and large hysteresis are of current interest.[10] It is now established that the interaction between SCO sites governs the bistability, while SCO itself is essentially a single molecule phenomenon. From this viewpoint, recent efforts have been devoted to design and synthesize SCO compounds exhibiting strong elastic interactions between spin-transition sites and multidimensional extended structure. Polymeric SCO compounds with bridging ligands[11] and mononuclear SCO compounds exhibiting intermolecular interactions such as hydrogen bonding and $\pi-\pi$ stacking[12] have been extensively investigated. Novel ligand systems that would provide not only SCO behavior but also have strong and extended enough elastic interactions between SCO sites are still most needed.

We have recently published a preliminary report on an unprecedented homochiral mixed-valence SCO complex, $[\mathrm{Fe^{II}H_3L}][\mathrm{Fe^{III}L}](\mathrm{NO_3})_2$, showing that the tripodal ligand $\mathrm{H_3L}$ (tris-[2-(((imidazol-4-yl)methylidene)amino)ethyl]amine) allows the SCO phenomenon for both the $\mathrm{Fe^{II}}$ and $\mathrm{Fe^{III}}$ oxidation states. Furthermore, the complex assumes a 2D extended sheet structure constructed by imidazole−imidazolate hydrogen bonds that yield extended interactions between SCO sites.[13] Here, we report the synthesis and properties of a whole series of SCO complexes with a tripod ligand containing three imidazoles, $[\mathrm{Fe^{II}H_3L^{Me}}](\mathrm{NO_3})_2\cdot 1.5\mathrm{H_2O}$ (**1**), $[\mathrm{Fe^{III}L^{Me}}]\cdot 3.5\mathrm{H_2O}$ (**2**), $[\mathrm{Fe^{II}H_3L^{Me}}][\mathrm{Fe^{II}L^{Me}}]\mathrm{NO_3}$ (**3**), and $[\mathrm{Fe^{II}H_3L^{Me}}][\mathrm{Fe^{III}L^{Me}}](\mathrm{NO_3})_2$ (**4**), where $\mathrm{H_3L^{Me}}$ = tris[2-(((2-methylimidazol-4-yl)methylidene)amino)ethyl]amine is the methyl substituted relative of $\mathrm{H_3L}$. The

---

(3) (a) Ohkoshi, S.; Hashimoto, K. *J. Am. Chem. Soc.* **1999**, *121*, 10591−10597. (b) Sato, O.; Iyoda, T.; Fujishima, A.; Hashimoto, K. *Science* **1996**, *272*, 704−705.

(4) (a) Coronado, E.; Galan-Mascaros, J. R.; Gomez-Garcia, C. J.; Laukhin, V. *Nature* **2000**, *408*, 447−449. (b) Takamatsu, N.; Akutagawa, T.; Hasegawa, T.; Nakamura, T.; Inabe, T.; Fujita, W.; Awaga, K. *Inorg. Chem.* **2000**, *39*, 870−871. (c) Imai, H.; Otsuka, T.; Naito, T.; Awaga, K.; Inabe, T. *J. Am. Chem. Soc.* **1999**, *121*, 8098−8103.

(5) Halder, G. J.; Kepert, C. J.; Moubaraki, B.; Murray, K. S.; Cashion, J. D. *Science* **2002**, *298*, 1762−1765.

(6) (a) Caneschi, A.; Gatteschi, D.; Sessoli, R. *Acc. Chem. Res.* **1989**, *22*, 393−398. (b) Miller, J. S.; Epstein, A. J.; Reiff, W. M. *Chem. Rev.* **1988**, *88* (8), 201−220. (c) Mallah, T.; Thiebaut, S.; Verdaguer, M.; Veillet, P. *Science* **1993**, *262*, 1554−1557. (d) Miyasaka, H.; Matsumoto, N.; Okawa, H.; Re, N.; Gallo, E.; Floriani, C. *J. Am. Chem. Soc.* **1996**, *118*, 981−994. (e) Matsumoto, N.; Sunatsuki, Y.; Miyasaka, H.; Hashimoto, Y.; Luneau, D.; Tuchagues, J.-P. *Angew. Chem., Int. Ed.* **1999**, *38*, 171−173. (f) Miyasaka, H.; Ieda, H.; Matsumoto, N.; Re, N.; Crescenzi, R.; Floriani, C. *Inorg. Chem.* **1998**, *37*, 255−263.

(7) (a) Irie, M. *Chem. Rev.* **2000**, *100*, 1685−1716. (b) Irie, M.; Fukaminato, T.; Sasaki, T.; Tamai, N.; Kawai, T. *Nature* **2002**, *420*, 759−760. (c) Itkis, M. E.; Chi, X.; Cordes, A. W.; Haddon, R. C. *Science* **2002**, *296*, 1443−1445.

(8) (a) König, E. *Prog. Inorg. Chem.* **1987**, *35*, 527−623. (b) König, E. *Struct. Bonding* (*Berlin*) **1991**, *76*, 51. (c) Goodwin, H. A. *Coord. Chem. Rev.* **1976**, *18*, 293−325. (d) Gütlich, P.; Hauser, A.; Spiering, H. *Angew. Chem., Int. Ed. Engl.* **1994**, *33*, 2024−2054. (e) Trofimenko, S. *Chem. Rev.* **1993**, *93*, 943. (f) Bousseksou, A.; Verelst, M.; Constant-Machado, H.; Lemercier, G.; Tuchagues, J.-P.; Varret, F. *Inorg. Chem.* **1996**, *35*, 110−115. Lemercier, G.; Verelst, M.; Bousseksou, A.; Varret, F.; Tuchagues, J.-P. In *Magnetism: A Supramolecular Function*; NATO ASI Series, Series C; Kahn, O., Ed.; Kluwer: Dordrecht, 1996; Vol. 484, pp 335−356.

(9) (a) Decurtins, S.; Gütlich, P.; Kohler, C. P.; Spiering, H.; Hauser, A. *Chem. Phys. Lett*. **1984**, *105*, 1−4. (b) Decurtins, S.; Gütlich, P.; Hasselbach, K. M.; Hauser, A.; Spiering, H. *Inorg. Chem.* **1985**, *24*, 2174−2178. (c) Gütlich, P.; Garcia, Y.; Woike, T. *Coord. Chem. Rev.* **2001**, *219*−*221*, 839−879.

(10) (a) Kahn, O.; Martinez, J. C. *Science* **1998**, *279*, 44−48. (b) van Koningsbruggen, P. J.; Garcia, Y.; Kahn, O.; Fournes, L.; Kooijman, H.; Spek, A. L.; Haasnoot, J. G.; Moscovici, J.; Provost, K.; Michalowicz, A.; Renz, F.; Gütlich, P. *Inorg. Chem.* **2000**, *39*, 1891−1900. (c) Real, J. A.; Andres, E.; Munoz, M. C.; Julve, M.; Granier, T.; Bousseksou, A.; Varret, F. *Science* **1995**, *268*, 265−267.

(11) (a) Letard, J.-F.; Guionneau, P.; Rabardel, L.; Howard, J. A. K.; Goeta, A. E.; Chasseau, D.; Kahn, O. *Inorg. Chem.* **1998**, *37*, 4432−4441. (b) Garcia, Y.; Kahn, O.; Rabardel, L.; Chansou, B.; Salmon, L.; Tuchagues, J.-P. *Inorg. Chem.* **1999**, *38*, 4663−4670. (c) Breuning, E.; Ruben, M.; Lehn, J.-M.; Renz, F.; Garcia, Y.; Ksenofontov, V.; Gütlich, P.; Wegelius, E.; Rissanen, K. *Angew. Chem., Int. Ed.* **2000**, *39*, 2504−2507. (d) Moliner, N.; Munoz, C.; Letard, S.; Solans, X.; Menendez, N.; Goujon, A.; Varret, F.; Real, J. A. *Inorg. Chem.* **2000**, *39*, 5390−5393. (e) Reger, D. L.; Little, C. A.; Rheingold, A. L.; Lam, M.; Liable-Sands, L. M.; Rhagitan, B.; Concolino, T.; Mohan, A.; Long, G. J.; Briois, V.; Grandjean, F. *Inorg. Chem.* **2001**, *40*, 1508−1520.

(12) (a) Hayami, S.; Gu, Z.; Shiro, M.; Einaga, A.; Fujishima, A.; Sato, O. *J. Am. Chem. Soc.* **2000**, *122*, 7126−7127. (b) Hayami, S.; Gu, Z.; Yoshiki, H.; Fujishima, A.; Sato, O. *J. Am. Chem. Soc.* **2001**, *123*, 11644−11650. (c) Boca, R.; Boca, M.; Dihan, L.; Falk, K.; Fuess, H.; Haase, W.; Jarosciak, R.; Papankova, B.; Renz, F.; Vrbova, M.; Werner, R. *Inorg. Chem.* **2001**, *40*, 3025−3033.

(13) Sunatsuki, Y.; Ikuta, Y.; Matsumoto, N.; Ohta, H.; Kojima, M.; Iijima, S.; Hayami, S.; Maeda, Y.; Kaizaki, S.; Dahan, F.; Tuchagues, J. P. *Angew. Chem., Int. Ed.* **2003**, *42*, 1614−1618.

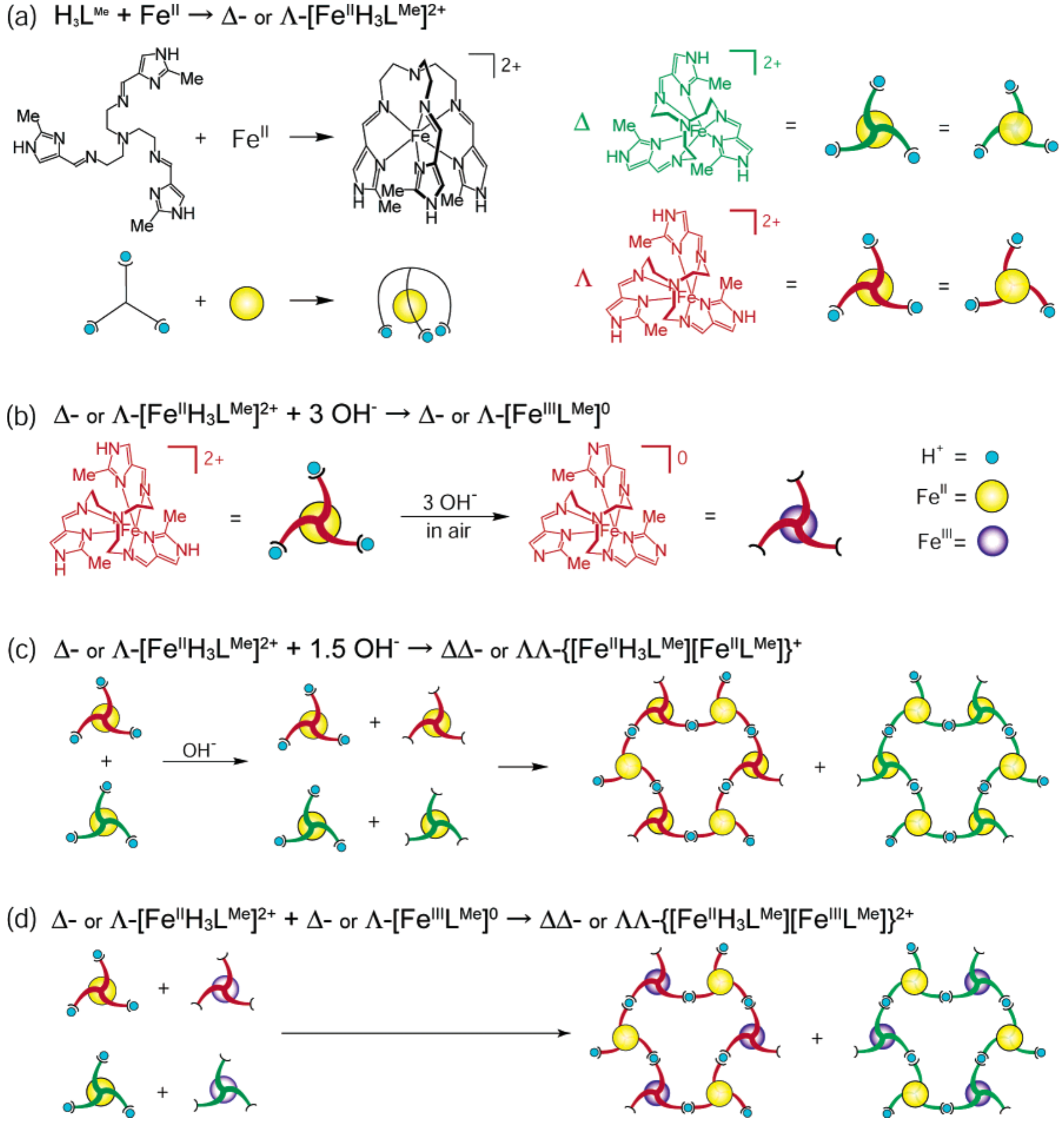

Figure 1. Schematic drawings of the synthetic procedures. (a) From the achiral components of ligand H_3L^{Me} and Fe^{II} ion to the isolated chiral molecule $[Fe^{II}H_3L^{Me}]^{2+}$ (**1**) ($H_3L^{Me} + Fe^{II} \rightarrow \Delta$- or Λ-$[Fe^{II}H_3L^{Me}]^{2+}$). Coordination of the achiral tripod ligand to the transition metal ion yields Δ (clockwise, green) and Λ (anticlockwise, red) chiral molecules, due to the screw coordination arrangement. (b) Deprotonation at the imidazole moieties of $[Fe^{II}H_3L^{Me}]^{2+}$ through addition of 3 equiv of aqueous KOH solution in air gradually generates $[Fe^{III}L^{Me}]^0$ (**2**) ($[Fe^{II}H_3L^{Me}]^{2+} + 3OH^- \rightarrow [Fe^{III}L^{Me}]^0$). (c) Deprotonation of $[Fe^{II}H_3L^{Me}](NO_3)_2$ (**1**) through addition of 1.5 equiv of KOH in MeOH yields a 2D compound $[Fe^{II}H_3L^{Me}][Fe^{II}L^{Me}]NO_3$ (**3**) (Δ- or Λ-$[Fe^{II}H_3L^{Me}]^{2+} + 1.5OH^- \rightarrow \{\Delta\Delta\text{-}[Fe^{II}H_3L^{Me}][Fe^{II}L^{Me}]\}^{+}{}_{\infty}$ or $\{\Lambda\Lambda\text{-}[Fe^{II}H_3L^{Me}][Fe^{II}L^{Me}]\}^{+}{}_{\infty}$). The chiral complementary complex ions generated during the deprotonation reaction, Δ- or Λ-$[Fe^{II}H_3L^{Me}]^{2+}$ and Δ- or Λ-$[Fe^{II}L^{Me}]^-$, assemble into homochiral 2D sheets, based on a hexameric repeat unit. The organization process is accompanied by intermolecular homochiral discrimination between $[Fe^{II}H_3L^{Me}]^{2+}$ and $[Fe^{II}L^{Me}]^-$ to produce an extended homochiral 2D sheet constructed by imidazole−imidazolate hydrogen bonds. (d) The simple mixing of **1** and **2** with a 1:1 molar ratio in MeOH yields the mixed-valence compound $[Fe^{II}H_3L^{Me}][Fe^{III}L^{Me}](NO_3)_2$ (**4**) (Δ- or Λ-$[Fe^{II}H_3L^{Me}]^{2+}$ + Δ- or Λ-$[Fe^{III}L^{Me}]^0 \rightarrow \{\Delta\Delta\text{-}[Fe^{II}H_3L^{Me}][Fe^{III}L^{Me}]\}^{2+}{}_{\infty}$ or $\{\Lambda\Lambda\text{-}[Fe^{II}H_3L^{Me}][Fe^{III}L^{Me}]\}^{2+}{}_{\infty}$).

complexes in this series assume various oxidation states and degrees of deprotonation, thus allowing us to investigate the effects of the degree of deprotonation and of the 2-methylimidazole substituent, on the iron oxidation and spin states.

Results and Discussion

Synthesis and Characterization. Figure 1 shows the schemes of the synthetic procedure for the family of SCO complexes **1**−**4**. The tripodal hexadentate ligand with N_6 donor atoms H_3L^{Me} was prepared by the condensation reaction of tris(2-aminoethyl)amine and 2-methyl-4-formylimidazole in a 1:3 molar ratio in methanol. The Fe^{II} complex with the neutral ligand, $[Fe^{II}H_3L^{Me}](NO_3)_2{\cdot}1.5H_2O$ (**1**), can be synthesized by two methods, A and B. Fe^{II} complex **1** was obtained as red-orange crystals by mixing the ligand H_3L^{Me}, $Fe^{II}Cl_2{\cdot}4H_2O$, and $NaNO_3$ at the molar ratio of 1:1:3 in methanol in aerobic conditions (method A). Alternatively, this compound can be obtained from the reaction of H_3L^{Me} with $Fe^{III}(NO_3)_3{\cdot}9H_2O$. A methanolic solution of $Fe^{III}(NO_3)_3{\cdot}9H_2O$ was added to a solution of the ligand, and the resulting mixture was allowed to stand for several days under acidic condition (ca. pH = 3), during which time well-grown red-orange crystals precipitated (method B). This alternative synthetic procedure demonstrated that, in the presence of the neutral tripod ligand, the Fe^{III} ion is reduced to Fe^{II}, even in aerobic conditions: the Fe^{II} complex with the neutral ligand is stabilized under acidic condition. Our several attempts to isolate the Fe^{III} complex with the neutral ligand have been unsuccessful, while the corresponding Fe^{III} complex with the unsubstituted neutral ligand $[Fe^{III}H_3L](ClO_4)_3$ is obtained.[14]

As previously demonstrated for the analogous compounds, $[Fe^{II}H_3L][Fe^{III}L](NO_3)_2$, $[Cu^{II}H_3L][Cu^{II}L]NO_3$, and $[Co^{III}H_3L][Co^{III}L](ClO_4)_3$ (H_3L = tris[2-(((imidazol-4-yl)methylidene)amino]ethyl)amine),[13,15] the synthetic procedure for preparing $[Fe^{II}H_3L^{Me}][Fe^{II}L^{Me}]NO_3$ (**3**) and $[Fe^{II}H_3L^{Me}][Fe^{III}L^{Me}](NO_3)_2$ (**4**) should involve an assembly process in which extended imidazole−imidazolate hydrogen bonding between the species with the neutral ligand and with the deprotonated ligand constitutes the driving force for the construction of homochiral 2D sheets (see Figure 1c,d). Addition of an aqueous KOH solution to the Fe^{II} complex with the neutral ligand form $[Fe^{II}H_3L^{Me}](NO_3)_2{\cdot}1.5H_2O$ (**1**) in methanol (1:1.5 ratio) in aerobic conditions yielded dark red crystals with the formula $[Fe^{II}H_3L^{Me}][Fe^{II}L^{Me}]NO_3$ (**3**). The acid−base conversion of one-half of the $[Fe^{II}H_3L^{Me}]^{2+}$ cations to $[Fe^{II}L^{Me}]^-$ anions that yields complex **3** is initiated by the addition of KOH. The $[Fe^{II}H_3L^{Me}]^{2+}$ and $[Fe^{II}L^{Me}]^-$ species assemble together through imidazole−imidazolate hydrogen bonds yielding an alternate array of protonated and deprotonated ferrous building units resulting in the 2D network of the crystal lattice described in the X-ray analysis. It is noticeable that the aerobic acid−base conversion of the $[Fe^{II}H_3L^{Me}]^{2+}$ cations was not associated with Fe^{II} to Fe^{III} oxidation, thus yielding the ferrous complex anions $[Fe^{II}L^{Me}]^-$. This is at variance with the case of the analogous H_3L tripodlike ligand without methyl groups which yielded the mixed-valence $[Fe^{II}H_3L][Fe^{III}L](NO_3)_2$ compound when the same reaction procedure was applied to the $[Fe^{II}H_3L](NO_3)_2$ complex. For this latter complex, the deprotonation and oxidation took place simultaneously, generating the fully deprotonated $[Fe^{III}L]^0$ species, which is hydrogen-bonded to the $[Fe^{II}H_3L]^{2+}$ component with the neutral ligand form to yield a 2D network structure built from $\{[Fe^{II}H_3L][Fe^{III}L]\}^{2+}$ units. These observations suggest that the oxidation state of iron coordinated to this type of tripodlike ligand is significantly affected not only by the imidazole deprotonation but also by the 2-imidazole substituent. The effect of the substituent on the oxidation state of iron was demonstrated by the cyclic voltammetry measurements. Both $[FeH_3L^{Me}]^{2+}$ and $[FeH_3L]^{2+}$ in methanol with 0.1 M $(n\text{-}C_4H_9)_4NBF_4$ showed a reversible redox wave assignable to the $Fe^{3+/2+}$ couple. The redox potential ($E°'$) for $[FeH_3L^{Me}]^{2+}$ (−0.011 V vs Ag/Ag$^+$ (0.01 M)) is less negative than $[FeH_3L]^{2+}$ ($E°' = -0.103$ V) by ca. 90 mV. Thus, it is clear that introduction of methyl groups at the 2-position of the imidazole rings in the tripod ligand stabilizes the Fe^{II} state.

When 3 equiv of aqueous KOH, anhydrous $Fe^{III}Cl_3$, and the ligand were mixed in methanol or when 3 equiv of aqueous KOH was added to a methanolic solution of **1**, and then the filtrate was allowed to stand for several days in the open air, the color of the solution gradually changed from yellow-orange to blue, and finally, a blue-black crystalline precipitate of the fully deprotonated ferric compound **2** with the chemical formula $[Fe^{III}L^{Me}]{\cdot}3.5H_2O$ deposited.

While the mixed-valence complex with the methyl-substituted ligand $[Fe^{II}H_3L^{Me}][Fe^{III}L^{Me}](NO_3)_2$ (**4**) could not be obtained from the deprotonation reaction of **1** with 1.5 equiv of KOH, it was easily obtained as black microcrystals by mixing methanolic solutions of $[Fe^{II}H_3L^{Me}](NO_3)_2{\cdot}1.5H_2O$ (**1**) and $[Fe^{III}L^{Me}]{\cdot}3.5H_2O$ (**2**) in the 1:1 mol ratio. Since the change of iron oxidation state in compounds **1** and **2** is slow, as shown in the subsection entitled "Absorption Spectral Changes Driven by Deprotonation and Protonation", and since the expected mixed-valence compound should be sparingly soluble due to its 2D extended structure, crystallization of compound **4** occurred immediately by this synthetic procedure.

Infrared Spectra. The infrared (IR) spectra for the series of compounds **1**−**4** were measured at ambient temperature as KBr pellets. All IR spectra showed characteristic intense bands around 1600 cm^{-1} assignable to the C═N stretching vibration of the Schiff-base ligand.[16] Compounds **1** (H_3L^{Me} HS-Fe^{II} at 295 K) and **2** (L^{Me} mainly LS-Fe^{III} at 295 K) (see subsection entitled "Magnetic Properties") exhibit a single sharp band due to the C═N stretching vibration of the tripodlike Schiff-base ligand at 1644 and 1601 cm^{-1}, respectively.[13,14] The IR spectrum of the mixed-valence compound **4** shows bands at 1634 and 1614 cm^{-1}, which are assigned to the ν(C═N) frequency of $[Fe^{II}H_3L^{Me}]^{2+}$ and $[Fe^{III}L^{Me}]^0$, respectively. The IR spectrum of **3** shows a deformed band around 1637 cm^{-1}. The C═N stretching vibration of the Schiff-base ligand is thus sensitive to both the oxidation and spin states of iron, and this C═N absorption may thus be a good probe for monitoring the SCO behavior.[17]

Absorption Spectra of $[Fe^{II}H_3L^{Me}](NO_3)_2{\cdot}1.5H_2O$ (1) and $[Fe^{III}L^{Me}]{\cdot}3.5H_2O$ (2) in Methanol. The electronic spectra of **1** and **2** recorded in methanol at 20 °C are shown in Figure 2. The spectrum of **1** exhibits an intense band in the visible region with an absorption maximum at λ_{max} = 428 nm (ϵ = 1090 M^{-1} cm^{-1}), which can be assigned to MLCT. In the near-IR region, the spectrum exhibits a weak band at λ_{max} = 870 nm (ϵ = 10 M^{-1} cm^{-1}), which can be assigned to the $^5T_2 \rightarrow {}^5E$ transition of HS-Fe^{II}.[18] If the Fe^{II} component was converted from the HS to the LS state, on

---

[14] Sunatsuki, Y.; Sakata, M.; Matsuzaki, S.; Matsumoto, N.; Kojima, M. *Chem. Lett.* **2001**, 1254−1255.

[15] (a) Katsuki, I.; Motoda, Y.; Sunatsuki, Y.; Matsumoto, N.; Nakashima, T.; Kojima, M. *J. Am. Chem. Soc.* **2002**, *124*, 629−640. (b) Sunatsuki, Y.; Motoda, Y.; Matsumoto, N. *Coord. Chem. Rev.* **2002**, *226*, 199−209. (c) Mimura, M.; Matsuo, T.; Motoda, Y.; Matsumoto, N.; Nakashima, T.; Kojima, M. *Chem. Lett.* **1998**, 691−692.

[16] Nakamoto, K. In *Infrared and Raman Spectra of Inorganic and Coordination Compounds*, 5th ed.; John Wiley and Sons: New York, 1997; Part B, Chapter III-14.

[17] (a) Zilverentant, C. L.; van Albada, G. A.; Bousseksou, A.; Haasnoot, J. G.; Reedijk, J. *Inorg. Chim. Acta* **2000**, *303*, 287−290. (b) Suemura, N.; Ohama, M.; Kaizaki, S. *Chem. Commun.* **2001**, 1538−1539.

[18] (a) Hinek, R.; Spiering, H.; Schollmeyer, D.; Gütlich, P.; Hauser, A. *Chem. Eur. J.* **1996**, *2*, 1427−1434. (b) Hauser, A. *J. Chem. Phys.* **1991**, *94*, 2741−2748.

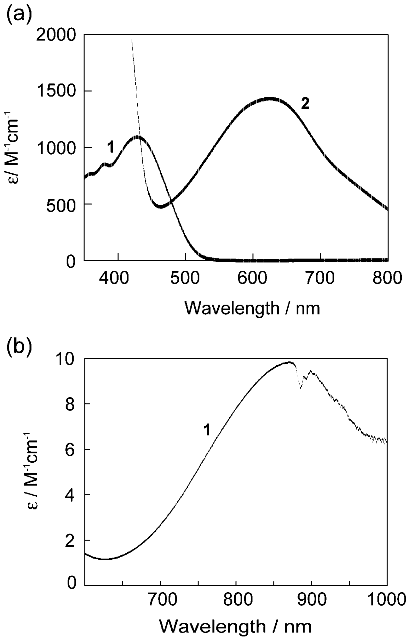

Figure 2. Electronic spectra of $[Fe^{II}H_3L^{Me}](NO_3)_2·1.5H_2O$ (**1**) and $[Fe^{III}L^{Me}]·3.5H_2O$ (**2**) in methanol at 20 °C.

the basis of the spectra reported for LS-Fe^{II} complexes with N_6 donor sets,[18] the $^1A_1 \rightarrow {}^1T_1$ and $^1A_1 \rightarrow {}^1T_2$ transitions of a potential LS-Fe^{II} component would appear around ca. 380 and 550 nm with molar extinction coefficients of ca. 30 M^{-1} cm^{-1}. They would thus be hidden by the intense MLCT bands already reported, and electronic spectroscopy thus cannot exclude the presence of a LS-Fe^{II} component. The magnetic moment of **1** in a ca. 1.0 M CD_3OD solution was thus measured by the Evans method: the $\chi_M T$ value of **1** at 297 K is 3.1 cm^3 K mol^{-1}, being consistent with the expected value for HS-Fe^{II}. The spectrum of **2** exhibits an intense band in the visible region at 625 nm ($\epsilon = 1430$ M^{-1} cm^{-1}), which can be assigned to the CT transition. The $\chi_M T$ value of **2** is 1.6 cm^3 K mol^{-1} at 297 K in the ca. 1.0 M CD_3OD solution. The value is intermediate between the spin-only values of HS and LS-Fe^{III} species (3:7 = HS/LS ratio evaluated on the basis of the spin-only values).

Absorption Spectral Change Driven by Deprotonation and Protonation. As shown in Figure 3, addition of aqueous NaOH (or KOH) to the methanolic solution of $[Fe^{II}H_3L^{Me}](NO_3)_2·1.5H_2O$ (**1**) did not yield any remarkable color change immediately, whereas the corresponding Fe^{II} complex without the 2-methyl imidazole substituent, $[Fe^{II}H_3L](NO_3)_2$, showed a drastic color change from orange-yellow to red-orange, green, and finally blue, immediately after addition of aqueous NaOH solution. The deprotonation process resulting from addition of NaOH was thus investigated with electronic spectroscopy, allowing us to discuss the deprotonation and substituent effects on the oxidation and spin states of iron in these complexes.

As shown in Figure 4a, the nonsubstituted complex $[Fe^{II}H_3L](NO_3)_2$ showed a drastic spectral change associated with the color change from yellow-orange to red-orange, green, and finally deep blue, with the addition of the 0.10 M NaOH solution, where each spectrum was measured immediately after every 0.075 mL of 0.10 M NaOH solution was added to 50 mL of the 0.5 mM methanol solution. The spectrum of $[Fe^{II}H_3L]^{2+}$ exhibits a broad band at 442 nm with $\epsilon = 1540$ M^{-1} cm^{-1} due to HS-$[Fe^{II}H_3L]^{2+}$. With the addition of the NaOH solution, the band shifted to a longer wavelength with a decrease of intensity, and bands appeared at ca. 540 and 650 nm. These bands indicate the formation of LS-$[Fe^{III}H_3L]^0$, because the isolated complex LS-$[Fe^{III}H_3L]^0$ exhibits bands at the same wavelengths with the same absorption coefficients. On the other hand, the spectrum of the methyl substituted compound **1** showed no drastic color change. The spectral changes of the methanolic solution of **1** with the addition of aqueous NaOH are shown in Figure 4b. The absorption spectrum of **1** in MeOH at 20 °C exhibits a broad band at $\lambda_{max} = 428$ nm with $\epsilon = 1090$ M^{-1} cm^{-1}. Upon addition of aqueous 0.10 M NaOH, the spectrum slightly changed, showing a distinct difference from the case of the nonsubstituted complex.

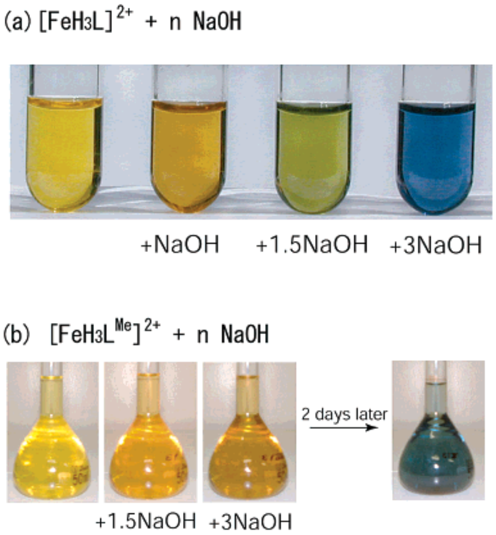

Figure 3. (a) Color change of the aqueous solution of $[Fe^{II}H_3L]^{2+}$ associated with the addition of aqueous NaOH solution. (b) Color change of the aqueous solution of $[Fe^{II}H_3L^{Me}]^{2+}$ associated with the addition of NaOH solution.

When the two solutions of **1** and 3 equiv of NaOH were mixed at once and the spectrum was recorded immediately, the mixed solution showed no band characteristic of $[Fe^{III}L^{Me}]^0$. The red color of the mixed solution changed very slowly to blue within several days at 20 °C in aerobic conditions. The time dependence of the spectrum of the mixed solution is shown in Figure 4c. The spectral changes are associated with isosbestic points at 433 and 496 nm. The intensity of the ca. 460 nm band decreases while the intensity of the ca. 620 nm band increases with time. The spectrum measured after 7 days showed a band at $\lambda_{max} = 622$ nm (ϵ = ca. 1100 M^{-1} cm^{-1}), the absorption maximum of which is characteristic of $[Fe^{III}L^{Me}]^0$, and the absorption coefficient is close to the value expected for **2** (see Figure 2a). The slightly smaller ϵ value is partly because oxidation from $[Fe^{II}L^{Me}]^{2+}$ to $[Fe^{III}L^{Me}]^0$ takes longer time and partly because the red sparingly soluble product **3** precipitates during the reaction.

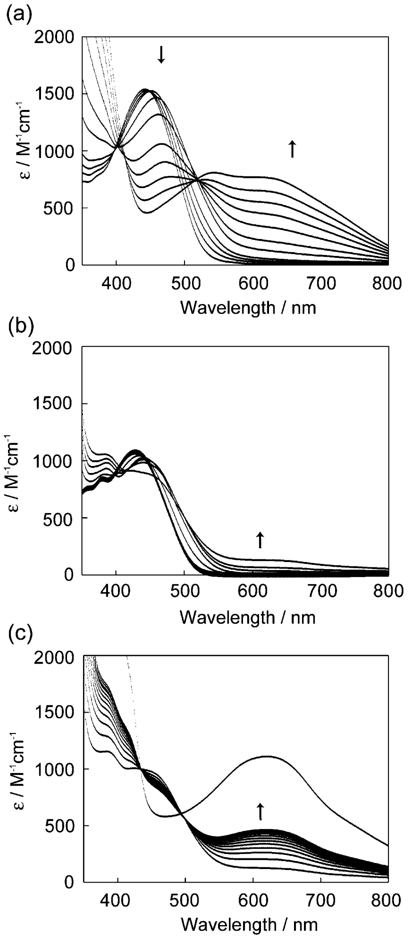

Figure 4. Deprotonation process from $[Fe^{II}H_3L]^{2+}$ to $[Fe^{III}L]^0$ and from $[Fe^{II}H_3L^{Me}]^{2+}$ to $[Fe^{III}L^{Me}]^0$. (a) Deprotonation process from $[Fe^{II}H_3L]^{2+}$ to $[Fe^{III}L]^0$, compared to that of the methyl-substituted complex. Electronic spectral change of $[Fe^{II}H_3L](NO_3)_2$ in MeOH upon addition of aqueous NaOH solution up to 3 equiv of NaOH. (b) Electronic spectral change of $[Fe^{II}H_3L^{Me}](NO_3)_2{\cdot}1.5H_2O$ (**1**) in MeOH with the addition of aqueous NaOH solution up to 3 equiv of NaOH. (c) Time dependence of the electronic spectrum of the mixed solution of 3 equiv of aqueous NaOH and **1**. Aqueous NaOH solution (3 equiv) was added at once to the methanolic solution of **1**. Spectra of the resulting solution were recorded every 2 h, and the final spectrum was recorded one week later.

The reverse reaction, a protonation process from $[Fe^{III}L^{Me}]^0$ to $[Fe^{II}H_3L^{Me}]^{2+}$, was also studied. The absorption spectrum of **2** in MeOH at 20 °C exhibits a broad band at $\lambda_{max} = 625$ nm with $\epsilon = 1430$ M^{-1} cm^{-1}. The spectrum of **2** changes immediately upon addition of aqueous HCl, and the spectral changes are shown in Figure 5a. When 1.5 equiv of 0.1 M HCl was added, the band at $\lambda_{max} = 625$ nm was split into two absorption bands at $\lambda_{max} = 526$ and 672 nm. Upon further addition of HCl, the band at 526 nm shifted to longer wavelength with an increase in intensity, and the second band at 672 nm disappeared. When 3 equiv of 0.1 M HCl was added, the spectrum exhibited a broad band at $\lambda_{max} = 564$ nm with $\epsilon = 2730$ M^{-1} cm^{-1} assigned to the $[Fe^{III}H_3L^{Me}]^{3+}$ species. The spectrum of the solution resulting from the 1:3 mixture of **2** and 0.1 M HCl slowly changed with time (Figure 5b). The band at $\lambda_{max} = 564$ nm decreased in intensity, and several days later the spectrum showed the band at ca. $\lambda_{max} = 420$ nm with $\epsilon = 785$ M^{-1} cm^{-1}, which is characteristic for $[Fe^{II}H_3L^{Me}]^{2+}$ (see Figure 2a).

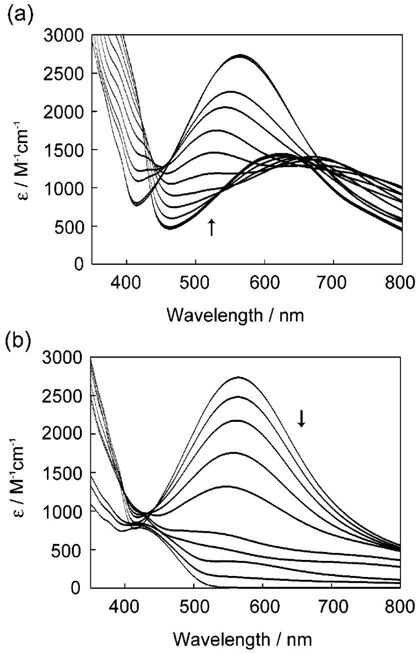

Figure 5. Protonation process from $[Fe^{III}L^{Me}]^0$ to $[Fe^{II}H_3L^{Me}]^{2+}$. (a) Absorption spectral change of $[Fe^{III}L^{Me}]{\cdot}3.5H_2O$ (**2**) in MeOH upon addition of aqueous 0.1 M HCl up to 3 equiv of HCl. (b) Time dependence of the electronic spectrum of the mixed solution of 3 equiv of aqueous HCl and **2**. Aqueous HCl (3 equiv) solution was added at once to the methanolic solution of **2**. The spectrum of the resulting solution was measured after the specified time (from upper, 0h, 3h, 8h, 16h, 1d, 2d, 3d, 4d, 5d, 7d).

Table 1. X-ray Crystallographic Data for $[Fe^{III}L^{Me}]{\cdot}3.5H_2O$ (**2**) at 293 K

formula	$FeC_{21}H_{34}N_{10}O_{3.5}$
fw	538.41
cryst syst	orthorhombic
space group	*Fdd*2
a, Å	23.129(6)
b, Å	35.387(6)
c, Å	12.513(4)
V, Å	10241.5(4)
Z	16
D_{calcd}, g cm^{-3}	1.397
μ(Mo Kα), cm^{-1}	6.34
λ (Å)	0.71069
R, R_w	0.063, 0.081
(Δ/ρ) max, min, e Å^{-3}	−0.45, +0.69

Structural Description of $[Fe^{III}L^{Me}]{\cdot}3.5H_2O$ (2). The ferric complex with the fully deprotonated ligand, **2**, crystallized in the orthorhombic space group *Fdd*2, with $[Fe^{III}L^{Me}]{\cdot}3.5H_2O$ as unique unit. The crystallographic data are summarized in Table 1. Selected bond distances, angles, and intermolecular contacts with their estimated standard deviations in parentheses are given in Table 2.

Figure 6 shows the dinuclear structure of **2** with the atom numbering scheme, in which two facing $[Fe^{III}L^{Me}]^0$ species are connected through three water molecules. The water oxygen atoms O(2), O(2)^A (generated by a symmetry operation of 2-fold rotation A; $1 - x, -y, -1 + z$), and O(4) bridge two adjacent $[Fe^{III}L^{Me}]$ and $[Fe^{III}L^{Me}]^A$ with interatomic distances O(2)···N(10) = 2.99(2) Å, O(2)···N(7)^A = 2.81(2) Å, O(4)···N(4) = 2.80(4) Å, and O(4)···N(4)^A = 2.93(3) Å. Considering the distances between the water oxygen and imidazolate nitrogen atoms, a hydrogen bonded dimeric structure is strongly suggested. The oxygen

Table 2. Relevant Bond Lengths (Å), Angles (deg), and Interatomic Contacts (Å) with Their Estimated Standard Deviations in Parentheses for $[Fe^{III}L^{Me}]\cdot 3.5H_2O$ (**2**)[a]

Bond Lengths (Å)			
Fe(1)−N(2)	2.03(1)	Fe(1)−N(3)	2.00(1)
Fe(1)−N(5)	2.01(1)	Fe(1)−N(6)	1.96(1)
Fe(1)−N(8)	1.98(1)	Fe(1)−N(9)	1.98(1)
Bond Angles (deg)			
N(2)−Fe(1)−N(3)	80.1(4)	N(2)−Fe(1)−N(5)	96.1(4)
N(3)−Fe(1)−N(5)	88.2(4)	N(2)−Fe(1)−N(6)	175.0(4)
N(3)−Fe(1)−N(6)	95.8(4)	N(5)−Fe(1)−N(6)	80.9(4)
N(2)−Fe(1)−N(8)	94.9(4)	N(3)−Fe(1)−N(8)	173.4(4)
N(5)−Fe(1)−N(8)	96.7(4)	N(6)−Fe(1)−N(8)	89.4(4)
N(2)−Fe(1)−N(9)	87.7(4)	N(3)−Fe(1)−N(9)	93.5(4)
N(5)−Fe(1)−N(9)	176.0(4)	N(6)−Fe(1)−N(9)	95.4(4)
N(8)−Fe(1)−N(9)	81.9(4)		
Interatomic Contacts (Å)			
$O(1)\cdots O(2)^B$	2.83(3)	$O(1)\cdots O(3)^B$	2.92(2)
$O(1)\cdots O(4)^D$	3.10(6)	$O(2)\cdots O(3)^C$	2.90(2)
$O(2)\cdots N(7)^A$	2.81(2)	$O(2)\cdots N(10)$	2.99(2)
$O(4)\cdots N(4)$	2.80(4)	$O(4)\cdots N(4)^A$	2.93(3)

[a] Symmetry operations: A, $1 - x, -y, -1 + z$; B, $-1/4 + x, -y + 1/4, z + 3/4$; C, $x + 1/4, -y + 1/4, z + 1/4$; D, $7/4 - x, y + 1/4, z - 1/4$.

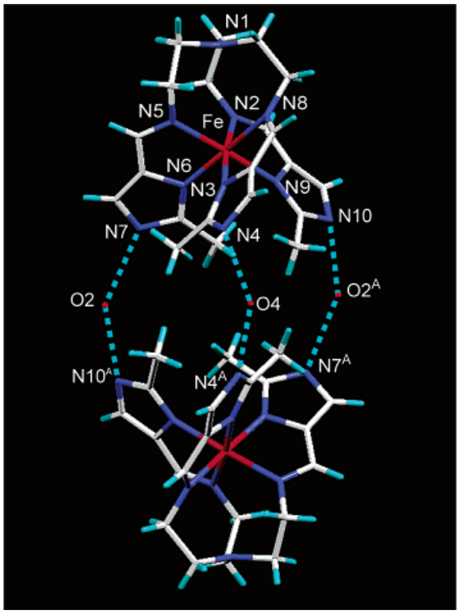

Figure 6. Dinuclear structure of $[Fe^{III}L^{Me}]\cdot 3.5H_2O$ (**2**) with atom numbering scheme.

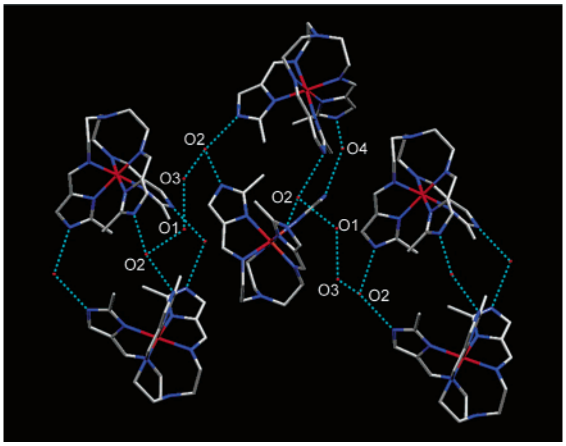

Figure 7. X-ray crystal structure of $[Fe^{III}L^{Me}]\cdot 3.5H_2O$ (**2**) showing the extended structure. The dinuclear units are further connected by other hydrogen bonds to form an extended structure.

Table 3. X-ray Crystallographic Data for $[Fe^{II}H_3L^{Me}][Fe^{II}L^{Me}]NO_3$ (**3**) at 293, 130, and 90 K

	293 K	130 K	90 K
formula	$C_{42}H_{57}Fe_2N_{21}O_3$	$C_{42}H_{57}Fe_2N_{21}O_3$	$C_{42}H_{57}Fe_2N_{21}O_3$
fw	1015.79	1015.79	1015.79
cryst syst	trigonal	trigonal	trigonal
space group	*R*3 (No. 146)	*R*3 (No. 146)	*R*3 (No. 146)
a, Å	12.093(2)	11.9312(17)	11.9031(18)
b, Å	12.093(2)	11.9312(17)	11.9031(18)
c, Å	28.350(3)	27.893(3)	27.742(3)
V, $Å^3$	3590.3(9)	3438.7(8)	3404.0(8)
Z	3	3	3
T, K	293 ± 2	130 ± 2	90 ± 2
D_{calcd}, g cm^{-3}	1.409	1.472	1.487
μ(Mo Kα), mm^{-1}	0.669	0.699	0.706
no. data collected	12042	11499	10345
no. unique data	4955	4735	4609
R(int)	0.0493	0.0452	0.0441
no. variable params	211	211	211
no. obsd reflms[a]	2200	2554	2495
R^b obsd, all	0.0491, 0.0970	0.0458, 0.0841	0.0440, 0.0811
$R_w{}^c$ obsd, all	0.1152, 0.1368	0.1063, 0.1206	0.0914, 0.1082
S	0.845	0.889	0.927
(Δ/ρ) max, min [e $Å^{-3}$]	0.795, −0.348	0.689, −0.325	0.577, −0.281

[a] Data with $F_o > 4\sigma(F_o)$. [b] $R = \Sigma||F_o| - |F_c||/\Sigma|F_o|$. [c] $R_w = [\Sigma w(|F_o{}^2| - |F_c{}^2|)^2/\Sigma w|F_o{}^2|^2]^{1/2}$.

atom O(2) is further hydrogen bonded to other water molecules with $O(1)\cdots O(2)^B = 2.83(3)$ Å (B; $-1/4 + x, -y + 1/4, z + 3/4$) and $O(2)\cdots O(3)^C = 2.90(2)$ Å (C; $x + 1/4, -y + 1/4, z + 1/4$) distances, and the oxygen atoms O(1) and O(3) are hydrogen bonded with an $O(1)\cdots O(3)^B = 2.92(2)$ Å distance, yielding an extended structure, as shown in Figure 7. The Fe−N(imine) and Fe−N(imidazolate) bond distances are in the 1.96(1)−2.03(1) Å range, as expected for LS-Fe^{III} complexes with N donor atoms.

Crystal Structure of $[Fe^{II}H_3L^{Me}][Fe^{II}L^{Me}]NO_3$ (3). The X-ray structural analysis of **3** was performed at 293, 130, and 90 K because the magnetic data demonstrated that the Fe^{II} sites of **3** are all in the HS state at 293 K, in the 1:1 HS/LS ratio at 130 K, and in the 1:3 HS/LS ratio at 90 K, respectively. The crystallographic data are summarized in Table 3. The crystal system and the space group are the same at all three temperatures. Selected bond distances, angles, and hydrogen bond distances with their estimated standard deviations in parentheses are given in Table 4.

First, we shall discuss the formulation of the complex with respect to the location of the imidazole hydrogen atom which could not be unambiguously located on the Fourier map as well as other hydrogen atoms. Consequently, all hydrogen atoms were geometrically placed at the calculated positions, and thus, the $[Fe^{II}H_3L^{Me}]^{2+}$ and $[Fe^{II}L^{Me}]^-$ components are not crystallographically distinguishable. Therefore, a homogeneous distribution of the imidazole hydrogen atoms over all ligands is also possible. However, on the basis of the X-ray results obtained for related complexes, we reached the conclusion that the $[Fe^{II}H_3L^{Me}]^{2+}[Fe^{II}L^{Me}]^-(NO_3)^-$ formulation is the most plausible. The imidazole hydrogen atom of the PF_6 salt, $[Fe^{II}H_3L^{Me}][Fe^{II}L^{Me}]PF_6$, was located on the D-Fourier map and well refined at the three temperatures for which the X-ray analyses were performed (295, 200, and

Table 4. Relevant Bond Lengths (Å), Angles (deg), and Hydrogen Bond Distances (Å) with Their Estimated Standard Deviations in Parentheses for $[Fe^{II}H_3L^{Me}][Fe^{II}L^{Me}]NO_3$ (**3**)[a]

	293 K	130 K	90 K
Bond Lengths (Å)			
Fe(1)−N(1)	2.171(4)	2.067(4)	2.031(3)
Fe(1)−N(2)	2.184(4)	2.095(3)	2.059(3)
Fe(2)−N(5)	2.173(4)	2.077(4)	2.065(3)
Fe(2)−N(6)	2.200(4)	2.107(3)	2.083(3)
N(1)−C(1)	1.279(7)	1.291(7)	1.295(5)
N(1)−C(6)	1.471(6)	1.470(6)	1.476(4)
N(2)−C(2)	1.369(6)	1.385(6)	1.391(5)
N(2)−C(4)	1.339(5)	1.334(5)	1.345(4)
N(5)−C(8)	1.272(6)	1.296(7)	1.289(5)
N(5)−C(13)	1.464(6)	1.482(6)	1.448(4)
N(6)−C(9)	1.374(6)	1.360(6)	1.375(5)
N(6)−C(11)	1.342(5)	1.344(5)	1.351(4)
Bond Angles (deg)			
N(1)−Fe(1)−N(2)	77.00(14)	79.41(14)	80.00(12)
N(1)−Fe(1)−N(1A)	97.93(13)	96.74(13)	96.31(10)
N(1)−Fe(1)−N(2A)	92.70(14)	91.25(14)	90.88(11)
N(1)−Fe(1)−N(2B)	168.79(15)	171.51(15)	172.26(13)
N(2)−Fe(1)−N(2A)	93.13(13)	93.05(13)	93.19(11)
N(5)−Fe(2)−N(6)	76.92(14)	78.74(14)	79.56(11)
N(5)−Fe(2)−N(5C)	98.30(12)	97.05(12)	96.30(10)
N(5)−Fe(2)−N(6C)	168.71(14)	170.96(14)	172.06(12)
N(5)−Fe(2)−N(6D)	92.54(14)	91.43(14)	90.92(11)
N(6)−Fe(2)−N(6C)	92.95(12)	93.29(12)	93.66(10)
Hydrogen Bonds (Å, deg)			
N(7)···N(3)	2.691(5)	2.692(5)	2.694(3)
N(7)−H(7)···N(3)	144.9	142.6	143.9

[a] Symmetry operations: A, 1 − *y*, *x* − *y*, *z*; B, 1 − *x* + *y*, 1 − *x*, *z*; C, −*y*, −1 + *x* − *y*, *z*; D, 1 − *x* + *y*, −*x*, *z*.

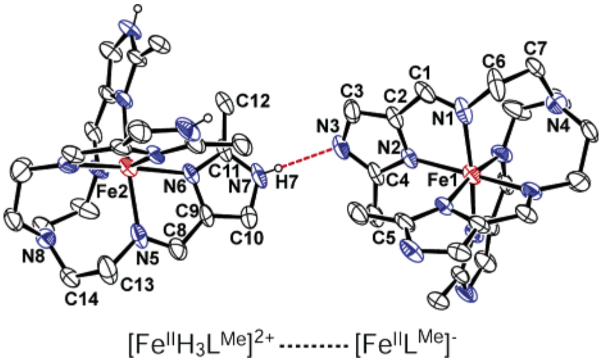

Figure 8. Crystal structure of $[Fe^{II}H_3L^{Me}][Fe^{II}L^{Me}]NO_3$ (**3**) at 293 K with atom numbering scheme.

100 K). On the basis of the Fe−N bond distances and N−Fe−N bond angles, the spin transition behavior of the two Fe^{II} sites is well revealed. The two-step SCO, {HS-$[Fe^{II}H_3L^{Me}]^{2+}$−HS-$[Fe^{II}L^{Me}]^-$} ↔ {HS-$[Fe^{II}H_3L^{Me}]^{2+}$−LS-$[Fe^{II}L^{Me}]^-$} ↔ {LS-$[Fe^{II}H_3L^{Me}]^{2+}$−LS-$[Fe^{II}L^{Me}]^-$}, was also observed by magnetic susceptibility measurements and Mössbauer spectroscopy. The results obtained for the PF_6 salt and several related complexes allow us to consider the $[Fe^{II}H_3L^{Me}]^{2+}[Fe^{II}L^{Me}]^-(NO_3)^-$ formulation as the most plausible.

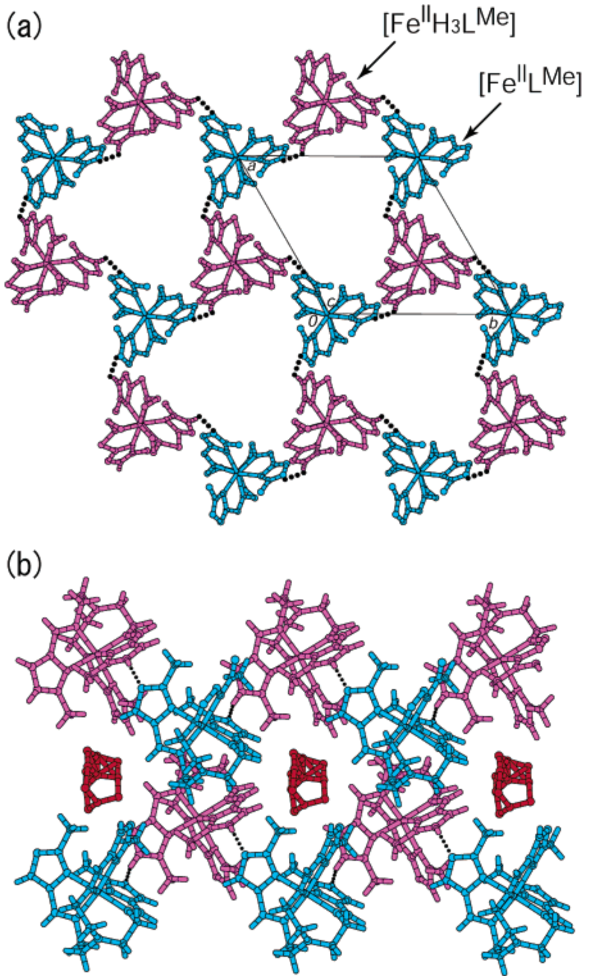

Figure 9. X-ray crystal structure of $[Fe^{II}H_3L^{Me}][Fe^{II}L^{Me}]NO_3$ (**3**) at 293 K. (a) Projection on the *ab*-plane showing a homochiral 2D sheet in which homochiral $[Fe^{II}H_3L^{Me}]^{2+}$ and $[Fe^{II}L^{Me}]^-$ species are linked by intermolecular imidazole−imidazolate hydrogen bonds. (b) Side view of a puckered sheet looking along the *a*-axis. In this 2D supramolecular structure, the capped tripodlike $[Fe^{II}H_3L^{Me}]^{2+}$ and $[Fe^{II}L^{Me}]^-$ components alternately array in an up-and-down mode. The anions are located between the sheets.

The crystal structure of **3** shown in Figure 8 consists of $[Fe^{II}H_3L^{Me}]^{2+}$ (Fe2) and $[Fe^{II}L^{Me}]^-$ (Fe1) complex ions hydrogen bonded through N−H···N contacts (imidazole hydrogen atom geometrically located), and one nitrate ion (not shown) disordered among several positions at all three temperatures. The $[Fe^{II}H_3L^{Me}]^{2+}$ and $[Fe^{II}L^{Me}]^-$ components are chiral with either a Δ (clockwise) or Λ (anticlockwise) configuration due to the screw coordination arrangement of the achiral tripod ligand around Fe^{II}. Each metal ion assumes an octahedral coordination environment with a N_6 donor set including three $Fe-N_{imine}$ and three $Fe-N_{imidazole}$ ($[Fe^{II}H_3L^{Me}]^{2+}$) bonds, or $Fe-N_{imidazolate}$ ($[Fe^{II}L^{Me}]^-$) bonds. The $[Fe^{II}H_3L^{Me}]^{2+}$ and $[Fe^{II}L^{Me}]^-$ components act as chiral complementary building units assembled into a 2D extended puckered sheet structure due to the imidazole−imidazolate hydrogen bonds. Figure 9 shows top (part a) and side (part b) views of the 2D layers. In this 2D supramolecular structure, the capped tripodlike components, $[Fe^{II}H_3L^{Me}]^{2+}$ and $[Fe^{II}L^{Me}]^-$, alternately array in an up-and-down mode yielding a homochiral extended 2D puckered layer based on a hexanuclear structure with a trigonal void as the repeat unit. Furthermore, the adjacent layers of like chirality are stacked to form a chiral crystal. These results indicate that spontaneous resolution took place during the course of the assembly reaction and crystallization.[19] Figure 10 shows the

---

(19) (a) Jacques, J.; Collet, A.; Wilen, S. H. *Enantiomers, racemates and resolutions*; John Wiley & Sons: New York, 1981. (b) Katsuki, I.; Matsumoto, N.; Kojima, M. *Inorg. Chem.* **2000**, *39*, 3350−3354.

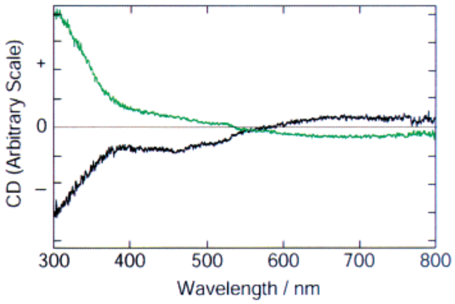

Figure 10. CD spectra of $[Fe^{II}H_3L^{Me}][Fe^{II}L^{Me}]NO_3$ (**3**) crystallites in KBr pellets at room temperature. The two KBr pellets were prepared using selected crystals and showed enantiomeric CD patterns, providing definitive evidence for spontaneous resolution.

enantiomeric circular dichroism (CD) spectra obtained from selected crystals, providing definitive evidence that spontaneous resolution has occurred.

The unit cell volume of 3590.3(9) Å^3 at 293 K is reduced to 3438.7(8) Å^3 at 130 K (4.2% reduction) with 2HS-Fe^{II} → HS-Fe^{II} + LS-Fe^{II} and to 3404.0(8) Å^3 at 90 K (5.3% reduction) with 2HS-Fe^{II} → $^1/_2$HS-Fe^{II} + $^3/_2$LS-Fe^{II}. The reduction of the unit cell volume can be compared with that of $[Fe^{II}H_3L^{Me}][Fe^{II}L^{Me}]PF_6$ exhibiting a perfect two-step spin transition, where the reduction of the unit cell volume is 4.0% with 2HS-Fe^{II} → HS-Fe^{II} + LS-Fe^{II} and 7.6% with 2HS-Fe^{II} → 2LS-Fe^{II}, respectively.

The Fe−N distances in $[Fe^{II}H_3L^{Me}]^{2+}$ and $[Fe^{II}L^{Me}]^-$ at 293 K are in the 2.171(4)−2.200(4) Å range, typical for HS-Fe^{II} bound to imine and imidazole nitrogen atoms. Upon temperature decrease from 293 to 130 K, the Fe−N distances shorten from 2.182 to 2.0865 Å, on average. Since the magnetic data at 130 K demonstrated that the Fe^{II} ions are in the 1:1 HS/LS ratio, it can be anticipated that the component $[Fe^{II}H_3L^{Me}]^{2+}$ remains in the HS state and $[Fe^{II}L^{Me}]^-$ converts to the LS state[13] upon cooling from 293 to 130 K and there should be noticeable differences in the Fe−N distances between $[Fe^{II}H_3L^{Me}]^{2+}$ and $[Fe^{II}L^{Me}]^-$ at 130 K. However, there is no remarkable difference in Fe−N bond distance between the two species at 130 K (the average Fe−N distance = 2.092 Å for Fe2 and 2.081 Å for Fe1). The difference between the average Fe−N distances at 293 and 130 K is 0.095 Å. The X-ray analysis of the PF_6 salt has shown that the average Fe−N distance of the $[Fe^{II}L^{Me}]^-$ component shortens by 0.179 Å while that of the $[Fe^{II}H_3L^{Me}]^{2+}$ component remains almost unchanged (0.006 Å) upon the 2HS-Fe^{II} → HS-Fe^{II} + LS-Fe^{II} SCO. The 0.095 Å value is nearly the average (0.179 + 0.006)/2 Å value. These facts suggest that the X-ray observation of the NO_3 salt, **3**, corresponds to an averaged structure, $\{[Fe^{II}H_3L^{Me}]^{2+} + [Fe^{II}L^{Me}]^-\}/2$.

At this stage, it is worth comparing this averaged structure to the related 2D compounds. (1) The X-ray analysis of the mixed-valence complex, $[Fe^{II}H_3L]^{2+}[Fe^{III}L]^0(NO_3)_2$, has evidenced four iron sites consisting of two pairs of $[Fe^{II}H_3L]^{2+}$ and $[Fe^{III}L]^0$ components with imidazole hydrogen atoms located on the D-Fourier map.[13] In this mixed-valence compound, there is no ambiguity about the association of L^{3-} with Fe^{III}, and about the proton location on the ferrous component. The $[Fe^{II}H_3L]^{2+}$ and $[Fe^{III}L]^0$ components alternately array in an up-and-down mode yielding a homochiral extended 2D puckered sheet. The puckered sheets stack along the *c*-axis to form crystals of the *P*3 space group. Along the *c*-axis, the components $[Fe^{II}H_3L]^{2+}$ and $[Fe^{III}L]^0$, which are involved into different 2D sheets, stack alternately, and the Fe atoms are located on C_3 axes. In this stacking arrangement (A), there are four unique Fe sites, because in addition to two Fe sites of an intra-2D sheet, there are two Fe sites of an inter-2D sheet along the *c*-axis. If the components $[Fe^{II}H_3L]^{2+}$ (or $[Fe^{III}L]^0$) stack along the *c*-axis, there must be two crystallographically unique Fe sites (B arrangement). (2) The X-ray analysis of another related mixed-valence compound, $[Fe^{II}H_3L]^{2+}[Fe^{III}L]^0(BF_4)_2$, has also been performed at several temperatures: at room temperature, there are six crystallographically unique Fe sites, that is three pairs of $[Fe^{II}H_3L]^{2+}$ and $[Fe^{III}L]^0$, i.e., three different sheets, but at lower temperatures there are only two Fe sites as a result of a $^1/_3$ reduction of the *c*-axis with regard to room temperature. The component species $[Fe^{II}H_3L]^{2+}$ and $[Fe^{III}L]^0$ alternately array in an up-and-down mode yielding a homochiral extended 2D puckered sheet. At room temperature, the component $[Fe^{II}H_3L]^{2+}$ of the first sheet, $[Fe^{III}L]^0$ of the second sheet, and $[Fe^{II}H_3L]^{2+}$of the third sheet are stacked alternately along the *c*-axis. As the result, there are three different layers consisting of $[Fe^{II}H_3L]^{2+}$, $[Fe^{III}L]^0$, and $\{[Fe^{II}H_3L]^{2+}$ and $[Fe^{III}L]^0\}$ components, respectively, when the structure was viewed perpendicular to the *c*-axis. At room temperature, the component species $[Fe^{II}H_3L]^{2+}$ and $[Fe^{III}L]^0$ are in the HS-Fe^{II} and LS-Fe^{III} states, respectively, and these two species can be easily distinguished due to the large difference in Fe−N distances and N−Fe−N angles. At lower temperature, HS-$[Fe^{II}H_3L]^{2+}$ converts to LS-$[Fe^{II}H_3L]^{2+}$, and the structural difference between LS-$[Fe^{II}H_3L]^{2+}$ and LS-$[Fe^{III}L]^0$ becomes smaller. As a result of the $[Fe^{II}H_3L]^{2+}$ SCO, the satellite peaks of the X-ray reflection data disappeared, and the *c*-axis was reduced to $^1/_3$ of its room temperature length. This result shows that two components of an intra-2D sheet as different as $[Fe^{II}H_3L]^{2+}$ and $[Fe^{III}L]^0$ as well as three Fe sites of three different sheets cannot be distinguished at low temperature.

On the basis of the related structures already described, it can be reasonably considered that the X-ray structure of **3** is suffering from such disorder due to the stacking manner. The plausible explanation is that there are two pairs of $[Fe^{II}H_3L^{Me}]^{2+}$ and $[Fe^{II}L^{Me}]^-$, i.e., two different sheets, and we are seeing the averaged structure: $\{[Fe^{II}H_3L^{Me}]^{2+}$(1st sheet) + $[Fe^{II}L^{Me}]^-$(2nd sheet)$\}/2$ + $\{[Fe^{II}L^{Me}]^{2+}$(1st sheet) + $[Fe^{II}H_3L^{Me}]^-$ (2nd sheet)$\}/2$. This type of situation may lead to a superlattice problem that has been often observed in one-dimensional compounds such as $[Pt^{II}(en)_2][Pt^{IV}X_2(en)_2]Y_4$ (X = Cl$^-$, Br$^-$, I$^-$; en = ethylenediamine; Y = ClO_4^-, BF_4^-) and layered crystals.[20] These facts demonstrate that the crystal structures of this series of 2D complexes tend to

---

(20) (a) Matsumoto, N.; Yamashita, M.; Kida, S.; Ueda, I. *Acta Crystallogr.* **1979**, *B35*, 1458−1460. (b) Yamashita, M.; Toriumi, K. *Inorg. Chim. Acta*, **1990**, *178*, 143−149. (c) Toriumi, K.; Yamashita, M.; Kurita, S.; Murase, I.; Ito, T. *Acta Crystallogr.* **1993**, *B49*, 497−506.

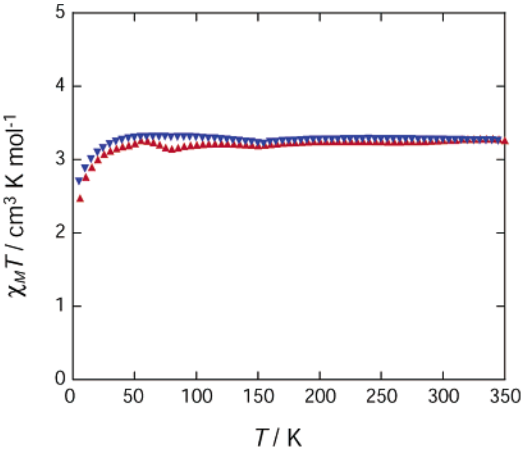

Figure 11. Magnetic behavior of $[Fe^{II}H_3L^{Me}](NO_3)_2·1.5H_2O$ (**1**) in the form of $\chi_M T$ vs T plots. The sample was quickly cooled from 300 to 5 K, and χ_M was successively measured in the warming (2−350 K, ▲) and cooling (350−2 K, ▼) modes, with a sweep rate of 1 K min^{-1}.

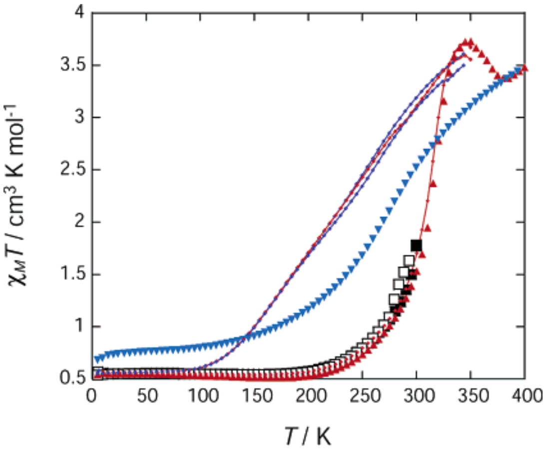

Figure 12. Magnetic behavior of $[Fe^{III}L]·3.5H_2O$ (**2**) in the form of the $\chi_M T$ vs T plots. The sample was quickly cooled from 300 to 5 K, and χ_M was measured in the warming and cooling modes. For three independent magnetic susceptibility experiments, the highest temperatures were set to 300 (□), 350 (△), and 400 (○) K, and a hydrated sample was used for each measurement. The $\chi_M T$ values were not corrected for removal of water molecules.

Table 5. Mössbauer Parameters for $[Fe^{II}H_3L^{Me}](NO_3)_2·1.5H_2O$ (**1**) and $[Fe^{III}L^{Me}]·3.5H_2O$ (**2**)

compd	T/K	δ^a/mm·s^{-1}	ΔE_Q/mm·s^{-1}	Γ^b/mm·s^{-1}
1	298	1.02	1.70	0.30, 0.26
	78	1.14	2.00	0.32, 0.30
2	298	0.15	1.39	0.39, 0.78
	78	0.22	1.79	0.27, 0.26

[a] Isomer shift data are reported to iron foil. [b] Full width at half-height.

have a serious disorder problem derived from the stacking arrangement of the 2D sheets. It is true that the ambiguity of the crystal structure could not in principle be fully solved: since the X-ray analysis is not effective enough to locate the imidazole hydrogen atom, the use of neutron diffraction analysis would be required to solve this problem.

Magnetic Properties of $[Fe^{II}H_3L^{Me}](NO_3)_2·1.5H_2O$ (1) and $[Fe^{III}L^{Me}]·3.5H_2O$ (2). The magnetic susceptibility of a polycrystalline sample of **1** was measured in the 2−350 K temperature range at 1 K min^{-1} sweeping rate under an applied magnetic field of 1 T. The sample was quickly cooled from room temperature down to 2 K, and as the first run, the magnetic susceptibility was measured in the warming mode from 2 to 350 K. Subsequently, the magnetic susceptibility was measured in the cooling mode from 350 to 2 K. The $\chi_M T$ versus T plots of **1** are shown in Figure 11. The magnetic behavior of **1** in the warming and cooling modes is very similar. Except for a slight decrease below 20 K, the $\chi_M T$ value per Fe is practically constant in the overall temperature range at ca. 3.2 cm^3 K mol^{-1}, as expected for HS-Fe^{II} ($S = 2$). The Mössbauer spectra of **1** were measured at 298 and 78 K, and the Mössbauer parameters are given in Table 5. Each spectrum consists of a doublet assignable to HS-Fe^{II}, being consistent with the magnetic susceptibility result.

The DSC measurement of $[Fe^{III}L^{Me}]·3.5H_2O$ (**2**) at the heating rate of 2 K min^{-1} showed a broad endothermic peak at 320−350 K and a rather sharp peak around 418 K. When a powdered sample of **2** was heated at the 5 K min^{-1} heating rate, a two-step weight loss was observed between 315 and 405 K, and the total weight loss in the TG curve was 11.9%, in agreement with the calculated weight percent of 3.5 water molecules per $[Fe^{III}L^{Me}]·3.5H_2O$ (**2**) (11.7%). In this two-step weight loss, a 6.9% weight loss corresponding to two water molecules (6.7%) was observed in the first dehydration process at 315−370 K, and a subsequent 5.0% weight loss corresponding to 1.5 water molecules (5.0%) was observed in the second dehydration process at 375−405 K. As demonstrated by the X-ray analysis, $[Fe^{III}L^{Me}]·3.5H_2O$ (**2**) involves two types of water molecules: 1.5 water molecules per $[Fe^{III}L^{Me}]·3.5H_2O$ play a binding role to form a dinuclear structure through three hydrogen bonds between the water molecules and the imidazolate nitrogen atoms of two adjacent complex molecules, and 2 water molecules participate in the formation of the extended network structure between the dinuclear components.

The magnetic susceptibility measurements of **2** were carried out taking into consideration its thermal properties and crystal structure, and the $\chi_M T$ versus T plots are shown in Figure 12. At first, the magnetic susceptibility of **2** was measured in the 5−300 K temperature range. The plots corresponding to the warming and subsequent cooling modes are nearly the same in this temperature range. The $\chi_M T$ value in the 5−200 K range is nearly constant at ca. 0.45 cm^3 K mol^{-1}. This value is compatible with the spin-only value for $S = {}^1/_2$, $g = 2.00$ (0.375 cm^3 K mol^{-1}), and is in the range reported for LS-Fe^{III}. Upon further warming, the $\chi_M T$ value increased to 1.8 cm^3 K mol^{-1} at 300 K, a value that is much smaller than the spin-only value for HS-Fe^{III}, $S = {}^5/_2$, $g = 2.00$ (4.37 cm^3 K mol^{-1}). The magnetic behavior of the sample in the subsequent 300−5 K cooling range was almost similar to that in the warming mode. The magnetic susceptibility of **2** was then measured in the 5−350 K temperature range. Upon warming, the $\chi_M T$ value increased from the 0.45 cm^3 K mol^{-1} LS value at 200 K to 3.8 cm^3 K mol^{-1} at 350 K, a value that is 0.58 cm^3 K mol^{-1} below the spin-only value for HS-Fe^{III}, $S = {}^5/_2$, $g = 2.00$ (4.37 cm^3 K mol^{-1}). Upon subsequent cooling of the sample from 350 K, the $\chi_M T$ value gradually decreased, reaching a plateau at 0.5 cm^3 K mol^{-1} (LS value) below 100 K. The difference in magnetic

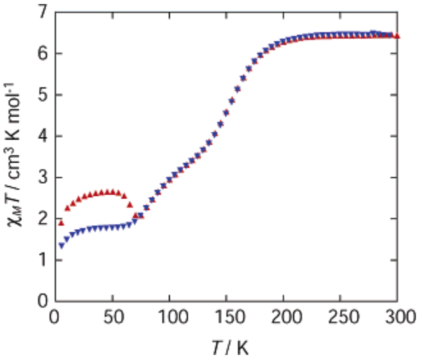

Figure 13. Magnetic behavior of $[Fe^{II}H_3L^{Me}][Fe^{II}L^{Me}]NO_3$ (**3**) in the form of the $\chi_M T$ vs T plots. The sample was quickly cooled from 300 to 5 K, and χ_M was successively measured in the warming (5−300 K, ▲) and cooling (300−5 K, ▼) modes, with a sweep rate of 1 K min^{-1}.

behavior between the warming and cooling mode may be ascribed to a dehydration process involving the two water molecules that participate in the formation of the extended network structure between dinuclear components. This hypothesis was confirmed by the fact that a further 5−350 K warming and cooling cycle yielded similar results. The magnetic susceptibility of **2** was finally measured in the 5−400 K temperature range. Upon warming from 5 K, the $\chi_M T$ value increased, reaching a maximum at 350 K, and then decreased, reaching a plateau at 370−400 K: the $\chi_M T$ decrease in the 350−400 K range is due to the second dehydration process. Upon cooling the sample from 400 K, the $\chi_M T$ value gradually decreased to the spin-only value for LS-Fe^{III}. The present observations further illustrate how weak intermolecular interactions through crystal solvent may significantly affect the SCO behavior.

The Mössbauer spectra of **2** were measured at 298 and 78 K, and the Mössbauer parameters are given in Table 5. The spectrum at 78 K consists of a doublet assignable to LS-Fe^{III}. The doublet of the spectrum at 298 K showed an asymmetric line-broadening, and its ΔE_Q became fairly smaller. This behavior would be characteristic of a spin flip rate comparable to the hyperfine frequency (10^7 to 10^8 s^{-1}),[21] suggesting the onset of spin transition at this temperature in accord with the magnetic results.

Magnetic Properties of $[Fe^{II}H_3L^{Me}][Fe^{II}L^{Me}]NO_3$ (3). The $\chi_M T$ versus T plots for **3** are shown in Figure 13 (χ_M is the molar magnetic susceptibility per 2Fe, and T is the absolute temperature). The magnetic behavior in the warming and cooling modes is very similar except below 70 K. Compound **3** showed no detectable thermal hysteresis in the SCO region. The difference in magnetic behavior below 70 K can be ascribed to the frozen-in effect, which is observed when the relaxation rate is slow due to cooperative interactions between SCO sites. The SCO behavior of **3** in the cooling mode (without the frozen-in effect) is described hereafter. In the 300−200 K region, the $\chi_M T$ value is nearly constant at ca. 6.7 cm^3 K mol^{-1}, as expected for two HS-Fe^{II} species ($S = 2$). Upon further cooling, in the 200−70 K region, the $\chi_M T$ value decreases and then reaches a plateau below 50 K. The inflection points at 115 and 80 K were obtained from the first derivative of the $\chi_M T$ versus T plots. The $\chi_M T$ value at the 115 K inflection point, 3.4 cm^3 K mol^{-1}, is approximately $^1/_2$ of 6.7 cm^3 K mol^{-1}. The $\chi_M T$ value in the plateau region below 50 K, 1.7 cm^3 K mol^{-1}, is approximately $^1/_4$ of 6.7 cm^3 K mol^{-1}. Since the $\chi_M T$ value expected for LS-Fe^{II} ($S = 0$) should be negligibly small compared with the value of the HS-Fe^{II} ($S = 2$), these magnetic susceptibility data suggest a two-step SCO involving, from higher to lower temperature: 4HS-Fe^{II} ↔ {2LS-Fe^{II} + 2HS-Fe^{II}} ↔ {3LS-Fe^{II} + HS-Fe^{II}}. Considering the $[Fe^{II}H_3L^{Me}][Fe^{II}L^{Me}]NO_3$ chemical formula of **3**, the magnetic susceptibility data thus suggest the presence of two $[Fe^{II}H_3L^{Me}]$-$[Fe^{II}L^{Me}]$ pairs: the $[Fe^{II}L^{Me}]$ deprotonated components would participate in the 4 HS-Fe^{II} ↔ {2 LS-Fe^{II} + 2 HS-Fe^{II}} step at 200−115 K, and one of the $[Fe^{II}H_3L^{Me}]^-$ protonated components would participate in the {2 LS-Fe^{II} + 2 HS-Fe^{II}} ↔ {3 LS-Fe^{II} + HS-Fe^{II}} step at 115−80 K. The fourth Fe^{II} site corresponding to the second $[Fe^{II}H_3L^{Me}]^-$ component would remain in the HS state. Two-step SCO processes have been reported for a few complexes, none of them involving four distinguishable Fe^{II} sites.[11,22]

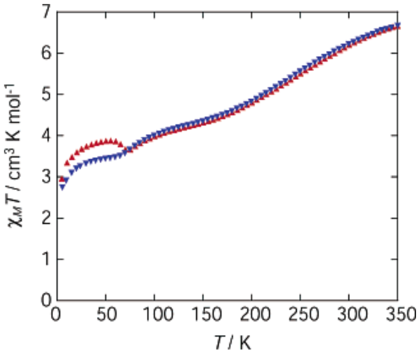

Figure 14. Magnetic behavior of $[Fe^{II}H_3L^{Me}][Fe^{III}L^{Me}](NO_3)_2$ (**4**) in the form of $\chi_M T$ vs T plots. The sample was quickly cooled from 300 to 5 K, and χ_M was successively measured in the warming (5−350 K, ▲) and cooling (350−5 K, ▼) modes, with a sweep rate of 1 K min^{-1}.

Magnetic Properties of $[Fe^{II}H_3L^{Me}][Fe^{III}L^{Me}](NO_3)_2$ (4). The $\chi_M T$ versus T plots in the 5−350 K temperature range are shown in Figure 14. The magnetic behavior in the warming and cooling modes is very similar except below 70 K and showed no detectable thermal hysteresis in the SCO region. The frozen-in effect observed below 70 K is probably due to cooperative effects resulting from the hydrogen-bonded 2D structure. The SCO behavior of **4** in the cooling mode (without the frozen-in effect) is described hereafter. Upon lowering the temperature from 350 K, the $\chi_M T$ value per 2Fe gradually and continuously decreases from 6.8 cm^3 K mol^{-1} at 350 K, then reaches a plateau region of ca. 3.3−3.0 cm^3 K mol^{-1} in the 70−20 K range, and finally decreases rather abruptly down to 2.5 cm^3 K mol^{-1} at 5 K. The $\chi_M T$ value of 6.8 cm^3 K mol^{-1} at 350 K, the highest

---

(21) (a) Lemercier, G.; Bousseksou, A.; Verelst, M.; Tuchagues, J.-P.; Varret, F. *J. Magn. Magn. Mater.* **1995**, *150*, 227−230. (b) Thiel, A.; Bousseksou, A.; Verelst, M.; Varret, F.; Tuchagues, J.-P. *Chem. Phys. Lett.* **1999**, *302*, 549−554 and references therein.

(22) (a) Boinnard, D.; Bousseksou, A.; Dworkin, A.; Savariault, J.-M.; Varret, F.; Tuchagues, J.-P. *Inorg. Chem.* **1994**, *33*, 271−281. (b) Letard, J.-F.; Real, J. A.; Moliner, N.; Gaspar, A. B.; Capes, L.; Cador, O.; Kahn, O. *J. Am. Chem. Soc.* **1999**, *121*, 10630−10631. (c) Simaan, A. J.; Boillot, M.-L.; Riviere, E.; Boussac, A.; Girerd, J.-J. *Angew. Chem., Int. Ed.* **2000**, *39*, 196−198.

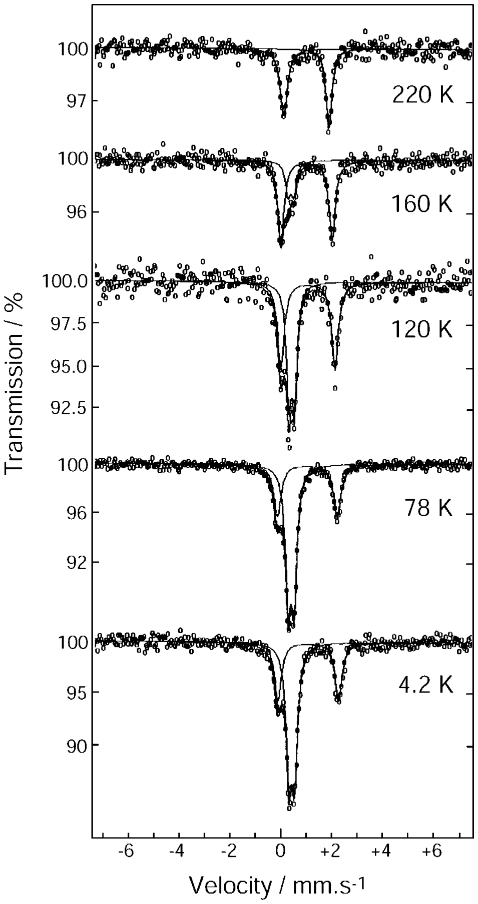

Figure 15. ^{57}Fe Mössbauer spectra of $[Fe^{II}H_3L^{Me}][Fe^{II}L^{Me}]NO_3$ (**3**) at selected temperatures. The spectra shown were recorded at 220, 160, 120, 78, and 4.2 K upon warming the sample after rapid cooling to 4.2 K.

temperature measured, is smaller than the spin-only value (7.37 cm^3 K mol^{-1}) expected for HS-Fe^{II} ($S = 2$) + HS-Fe^{III} ($S = {}^5/_2$) with $g = 2.00$. The $\chi_M T$ versus T plots show an inflection point at 220 K with a $\chi_M T$ value (5.4 cm^3 K mol^{-1}) very close to the spin-only value expected for (HS-Fe^{II} + $^1/_2$(HS + LS)Fe^{III}) (5.37 cm^3 K mol^{-1}). The $\chi_M T$ value in the 70−20 K plateau region (ca. 3.2 cm^3 K mol^{-1}) is close to the spin-only value expected for (HS-Fe^{II} + LS-Fe^{III}) (3.37 cm^3 K mol^{-1}). The magnetic susceptibility results described here suggest that the Fe^{III} site exhibits a gradual two-step spin transition in the 70 to ca. 400 K temperature range while the Fe^{II} site remains mainly in the HS state.

Mössbauer Spectroscopy. The temperature dependence of the Mössbauer spectra of compounds **3** and **4** was investigated in the 4.2−300 K range. The samples were initially rapidly cooled to 4.2 K, and Mössbauer spectra were measured at selected temperatures in the warming mode, and then in the cooling mode.

Mössbauer Spectra of $[Fe^{II}H_3L^{Me}][Fe^{II}L^{Me}]NO_3$ (3). The spectra obtained in the warming and cooling modes are nearly the same except for those below 50 K. Representative spectra are shown in Figure 15. In the 298−200 K temperature range, they consist of a doublet assignable to HS-Fe^{II} (isomer shift $\delta = 1.00$ mm s^{-1} and quadruple splitting $\Delta E_Q = 1.62$ mm s^{-1} at 298 K). Although two types of HS-Fe^{II} species would be expected at 298 K, $[Fe^{II}H_3L^{Me}]^{2+}$ and $[Fe^{II}L^{Me}]^-$, the Mössbauer spectra do not distinguish them. This behavior originates probably from a significant delocalization of the charges at the periphery of the bulky $[Fe^{II}H_3L^{Me}]^{2+}$ cations and $[Fe^{II}L^{Me}]^-$ anions, delocalization which is increased by the extended imidazole−imidazolate hydrogen bond network. This charge spreading (spatially similar for $[Fe^{II}H_3L^{Me}]^{2+}$ and $[Fe^{II}L^{Me}]^-$) is most probably responsible for a minimized difference in electronic structure of HS-iron(II) among the cationic and anionic components, yielding undistinguishable Mössbauer doublets. Below 200 K, the spectra consist of two quadruple-split doublets ($\delta = 1.10$ and 0.46 mm s^{-1}, $\Delta E_Q = 2.13$ and 0.23 mm s^{-1}, at 120 K) assigned to HS- and LS-Fe^{II}, respectively. A deconvolution analysis of the spectrum at each temperature was performed in order to determine the molar fraction of the HS-Fe^{II} versus total Fe^{II}. The resulting Mössbauer parameters are gathered in Table 6. The plots of the HS-Fe^{II} versus total Fe^{II} molar fraction derived from the Mössbauer spectra and the magnetic susceptibility measurements are shown in Figure 16. In agreement with the $\chi_M T$ versus T data, the plots in the warming and cooling modes are nearly the same except below 50 K. The difference below 50 K may be ascribed to the frozen-in effect due to the slow relaxation of the SCO

Table 6. Mössbauer Parameters for $[Fe^{II}H_3L^{Me}][Fe^{II}L^{Me}]NO_3$ (**3**)

T/K	δ^a/mm^{-1}	ΔE_Q/mm s^{-1}	Γ^b/mm s^{-1}	relative area/%
On Heating after Rapid Cooling to 4.2 K				
298	1.00	1.62	0.32, 0.26	100
250	1.03	1.72	0.36, 0.27	100
220	1.05	1.77	0.35, 0.27	100
200	1.05	1.84	0.30	94
	0.47	0.23	0.24	6
180	1.08	1.91	0.30	86
	0.48	0.25	0.24	14
160	1.09	2.00	0.31	76
	0.47	0.23	0.25	25
140	1.10	2.06	0.35	61
	0.47	0.23	0.24	39
120	1.10	2.13	0.32	51
	0.46	0.23	0.24	49
100	1.12	2.25	0.33	48
	0.48	0.22	0.24	52
78	1.12	2.34	0.35	36
	0.48	0.24	0.26	64
50	1.11	2.40	0.35	30
	0.48	0.23	0.28	70
25	1.11	2.38	0.34	37
	0.49	0.23	0.26	63
4.2	1.13	2.38	0.33	37
	0.49	0.23	0.27	63
On Slow Cooling from Room Temperature				
220	1.04	1.78	0.35, 0.26	100
160	1.08	2.00	0.31	77
	0.47	0.20	0.23	23
120	1.11	2.16	0.31	50
	0.47	0.21	0.26	50
100	1.11	2.27	0.34	47
	0.48	0.23	0.25	53
78	1.13	2.31	0.33	35
	0.48	0.23	0.26	65
50	1.13	2.38	0.34	26
	0.48	0.22	0.28	74
25	1.13	2.36	0.32	24
	0.48	0.24	0.28	76
4.2	1.14	2.37	0.33	26
	0.49	0.23	0.26	74

[a] Isomer shift data are reported to iron foil. [b] Full width at half-height.

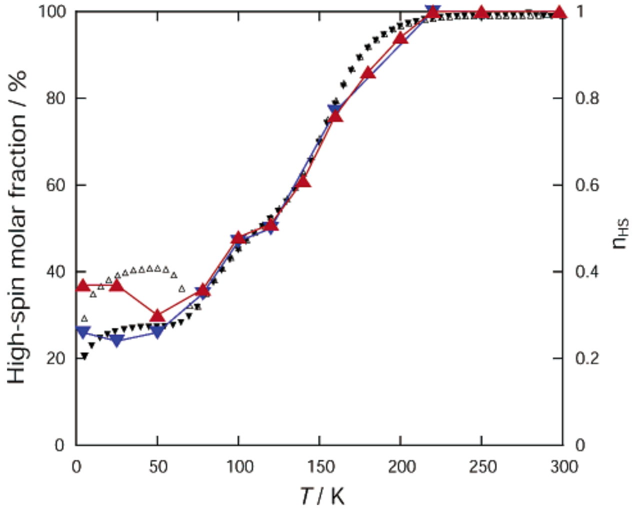

Figure 16. The HS-Fe^{II} vs total Fe^{II} molar fraction obtained by deconvolution analysis of each Mössbauer spectrum, together with the HS-Fe^{II} vs total Fe^{II} molar fraction obtained from magnetic susceptibility. For Mössbauer spectroscopy, the (▲) values were recorded upon warming the sample after rapid cooling to 4.2 K, and the (▼) values were recorded on subsequent slow cooling. The HS fraction n_{HS} from magnetic susceptibility was calculated by the equation $(\chi_M T)_{obs} = n_{HS}\,(\chi_M T)_{HS} + (1 - n_{HS})\,(\chi_M T)_{LS}$, with the following limiting values: $(\chi_M T)_{HS} = 6.7$ cm^3 K mol^{-1} and $(\chi_M T)_{LS} = 0.0$ cm^3 K mol^{-1}.

sites. The plot of the HS-Fe^{II} versus total Fe^{II} molar fraction in the cooling mode shows three plateau regions corresponding to molar fractions of 1.0 at 298−200 K, 0.5 at 120−110 K, and 0.25 at 50−4.2 K. The results of the Mössbauer study thus agree well with those from the magnetic susceptibility measurements.

Mössbauer Spectra of $[Fe^{II}H_3L^{Me}][Fe^{III}L^{Me}](NO_3)_2$ (4). The Mössbauer spectra in the warming and cooling modes are nearly the same except for those below 50 K. Representative spectra obtained in the warming mode are shown in Figure 17, which provides definitive evidence for the mixed-valence states. The spectrum at 298 K consists of a doublet assignable to HS-Fe^{II} ($\delta = 1.01$ mm s^{-1}, $\Delta E_Q =$ 1.69 mm s^{-1}) and peaks assignable to HS and LS-Fe^{III}. The spectrum at 78 K consists of two main quadruple-split doublets assigned to HS-Fe^{II} ($\delta = 1.12$ mm s^{-1}, $\Delta E_Q = 1.93$ mm s^{-1}) and LS-Fe^{III} ($\delta = 0.22$ mm s^{-1}, $\Delta E_Q = 1.76$ mm s^{-1}), and a low-intensity doublet attributable to LS-Fe^{II} ($\delta = 0.46$ mm s^{-1}, $\Delta E_Q = 0.23$ mm s^{-1}). The Fe^{II}/Fe^{III} area ratio at each temperature is very close to 1:1 in agreement with the Fe^{II}/Fe^{III} valence ratio expected from the chemical formula of **4**. In addition, the Mössbauer spectra clearly show the onset of the Fe^{II} spin transition below 120 K, and the incomplete nature of this HS-Fe^{II} → LS-Fe^{II} transition: indeed, 60−80% of the Fe^{II} sites remain HS below 50 K. A deconvolution analysis of the spectrum at each temperature was performed in order to determine the molar fraction of HS-Fe^{II} versus total Fe^{II}. The resulting Mössbauer parameters are gathered in Table 7. The results of the deconvolution analysis of the Mössbauer spectra of **4** yielding the molar fraction of HS-Fe^{II} versus total Fe^{II} are plotted versus temperature in Figure 18. In agreement with the $\chi_M T$ versus T data, the plots in the warming and cooling modes are nearly the same except below 50 K. The difference below 50 K (compare the 4.2 K spectra in Figure 17) may be ascribed to the frozen-in effect due to the slow relaxation of the spin-crossover sites. Upon raising the temperature above ca. 170 K, the Fe^{III} doublet begun to show an asymmetric line-broadening, and its ΔE_Q became somewhat smaller (0.90 mm s^{-1} at 298 K). This behavior is characteristic of a spin flip rate comparable to the hyperfine frequency (10^7 to 10^8 s^{-1}): the Mössbauer line shape then depends on the interstate conversion rate and the LS/HS ratio.[22]

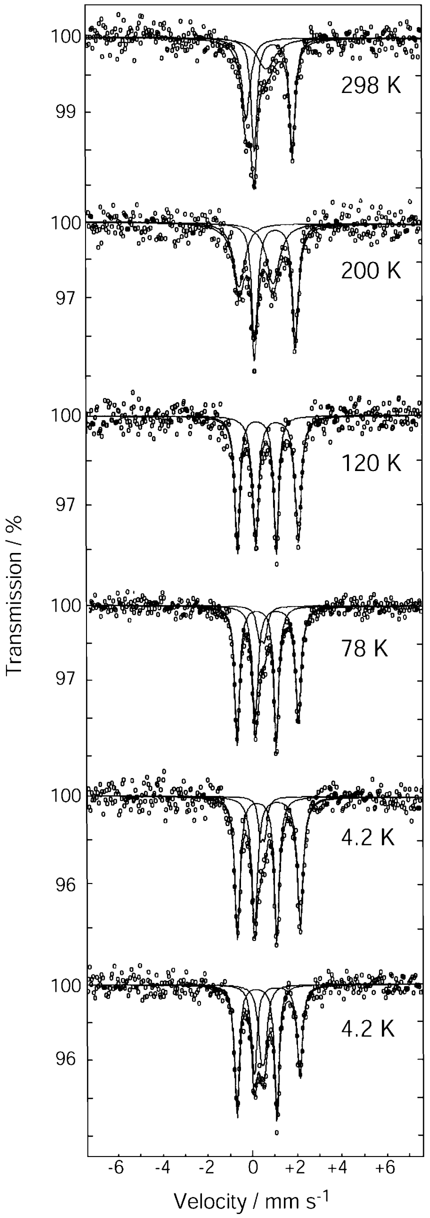

Figure 17. ^{57}Fe Mössbauer spectra of $[Fe^{II}H_3L^{Me}][Fe^{III}L^{Me}](NO_3)_2$ (**4**) at selected temperatures. The 4.2 (next to bottom), 78, 120, 200, and 298 K spectra were recorded upon warming the sample after rapid cooling to 4.2 K. The bottom 4.2 K Mössbauer spectrum was recorded after cooling the sample slowly.

LIESST and Reverse-LIESST Effects of $[Fe^{II}H_3L^{Me}]$-$[Fe^{II}L^{Me}]NO_3$ (3). Figure 19a shows the time dependence of the $\chi_M T$ value at 5 K upon green light irradiation ($\lambda_{max} =$ 500 nm). Light irradiation at 5 K produced an increase of the $\chi_M T$ value, which is attributed to the LS → HS spin transition at the Fe^{II} sites (light induced excited spin state

Table 7. Mössbauer Parameters for $[Fe^{II}H_3L^{Me}][Fe^{III}L^{Me}](NO_3)_2$ (**4**)

T/K	δ^a/mm s^{-1}	ΔE_Q/mm s^{-1}	Γ^b/mm s^{-1}	relative area/%
On Heating after Rapid Cooling to 4.2 K				
298	1.01	1.69	0.30	51
	0.23	0.90	0.45, 0.97	49
250	1.03	1.77	0.31	53
	0.21	1.02	0.48, 1.00	47
200	1.07	1.82	0.32	49
	0.21	1.53	0.60, 0.70	51
170	1.08	1.84	0.32	54
	0.19	1.67	0.35	46
120	1.11	1.91	0.33	53
	0.21	1.74	0.27	47
100	1.11	1.90	0.31	48
	0.51	0.23	0.27	7
	0.23	1.76	0.27	45
78	1.12	1.93	0.31	44
	0.46	0.23	0.28	11
	0.22	1.76	0.26	45
50	1.13	1.97	0.30	42
	0.51	0.19	0.29	11
	0.22	1.77	0.28	47
4.2	1.13	2.04	0.31	46
	0.47	0.20	0.24	10
	0.22	1.76	0.28	44
On Slow Cooling from Room Temperature				
120	1.10	1.90	0.33	52
	0.20	1.73	0.27	48
100	1.12	1.92	0.34	48
	0.51	0.25	0.27	7
	0.21	1.75	0.27	45
78	1.12	1.96	0.31	45
	0.46	0.18	0.30	11
	0.18	1.76	0.27	44
50	1.14	1.99	0.32	41
	0.49	0.23	0.27	15
	0.22	1.78	0.25	44
4.2	1.12	2.04	0.29	35
	0.49	0.19	0.29	22
	0.22	1.78	0.25	43

[a] Isomer shift data are reported to iron foil. [b] Full width at half-height.

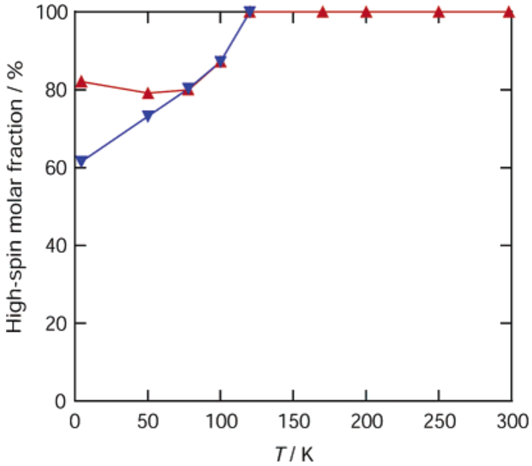

Figure 18. The HS-Fe^{II} vs total Fe^{II} molar fraction obtained by deconvolution analysis of each Mössbauer spectrum. The (▲) values were recorded upon warming the sample after rapid cooling to 4.2 K, and the (▼) values were recorded on subsequent slow cooling.

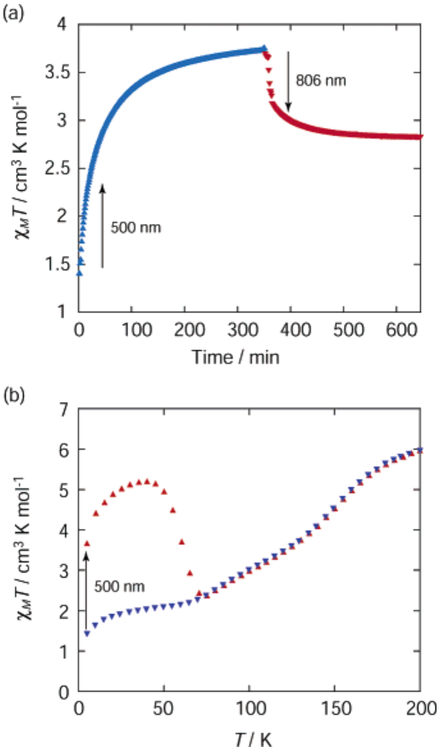

Figure 19. LIESST and reverse-LIESST of $[Fe^{II}H_3L^{Me}][Fe^{II}L^{Me}]NO_3$ (**3**). (a) Time dependence of the $\chi_M T$ value during irradiation with green (λ_{max} = 500 nm) and red (λ = 806 nm) light at 5 K, showing the LIESST and reverse-LIESST effects. (b) $\chi_M T$ vs T plots showing the LIESST effect and the relaxation process. After green light irradiation (λ_{max} = 500 nm) was switched off, the thermal relaxation process was recorded in the warming mode (▲), and then, the $\chi_M T$ value was measured in the cooling mode from 300 to 5 K (▼).

trapping (LIESST) effect). The sample was irradiated with green light at 5 K until the $\chi_M T$ value reached a saturation value and the green light was switched off. Subsequent irradiation with red laser light (λ_{max} = 806 nm) at 5 K induced a decrease of the $\chi_M T$ value, attributed to the HS → LS transition (reverse-LIESST effect); however, the $\chi_M T$ value did not perfectly reach the initial value (before irradiation with the green and red lights). The described experiments demonstrate that complex **3** presents the LIESST and partial reverse-LIESST effects. Though the d−d bands assigned to the LS-Fe^{II} state in this series of compounds are expected to be hidden by strong MLCT bands, they should be at ca. 380 and 550 nm, considering the Fe^{II} complexes with analogous N$_6$ donor atoms.[18] The electronic spectrum of $[Fe^{II}H_3L^{Me}](NO_3)_2{\cdot}1.5H_2O$ (**1**), a component of $[Fe^{II}H_3L^{Me}]$-$[Fe^{II}L^{Me}]NO_3$ (**3**), exhibits a weak d−d band with an absorption maximum at 870 nm (ϵ = 10 M^{-1} cm^{-1}) assigned to the $^5T_2 \rightarrow {}^5E$ transition of the HS-Fe^{II}. The red light irradiation (λ = 806 nm) would thus induce the $^5T_2 \rightarrow {}^5E$ transition allowing occurrence of the reverse-LIESST effect.

In another experiment, following irradiation of the sample up to saturation, the green light was switched off, and then, the thermal relaxation process was studied by monitoring the $\chi_M T$ value on warming the sample. Figure 19b shows the result. A progressive increase of $\chi_M T$ was observed as the sample was slowly warmed (1 K min^{-1}). The thermal dependence of $\chi_M T$ reaches a maximum value of 5.2 cm^3 K mol^{-1}. The reduced $\chi_M T$ values in the lowest temperature range most probably result from operation of zero-field splitting of the S = 2 ground state for the trapped HS molecules.

LIESST and Reverse-LIESST Effects of $[Fe^{II}H_3L^{Me}]$-$[Fe^{III}L^{Me}](NO_3)_2$ (4). Figure 20a shows the time dependence of the $\chi_M T$ value at 5 K upon green light irradiation (λ_{max} = 500 nm). Light irradiation produced an increase of the $\chi_M T$

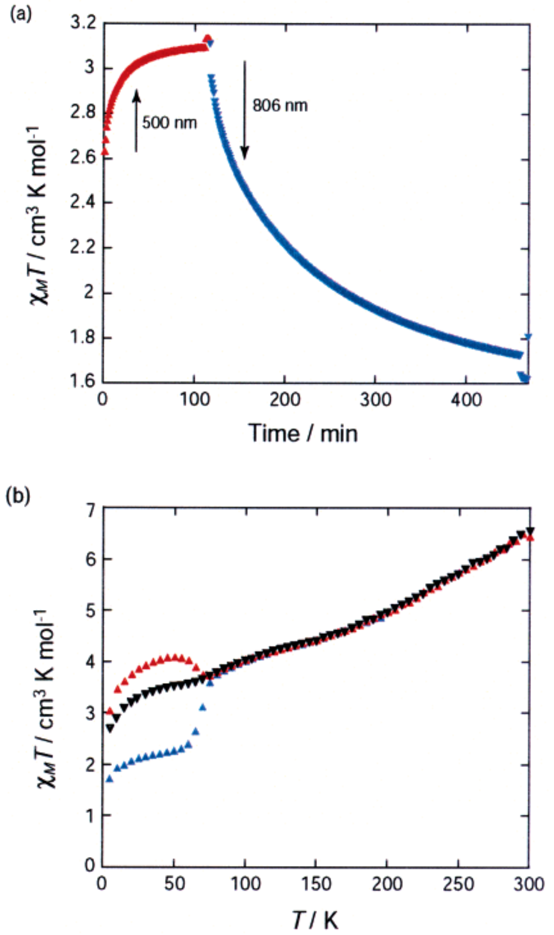

Figure 20. LIESST and reverse-LIESST of $[Fe^{II}H_3L^{Me}][Fe^{II}L^{Me}](NO_3)_2$ (**4**). (a) Time dependence of the $\chi_M T$ value during irradiation with green (500 nm) and red (806 nm) light at 5 K, showing the LIESST and reverse-LIESST effects. (b) $\chi_M T$ vs T plots showing the thermal relaxation after the LIESST and reverse-LIESST effects. The thermal relaxation process was recorded in the warming mode (▲) after green light irradiation and after red light irradiation. After the relaxation process, the $\chi_M T$ value was measured in the cooling mode from 300 to 5 K (▼).

value from 2.6 cm^3 K mol^{-1} up to 3.1 cm^3 K mol^{-1}. In the case of the mixed-valence compound **4**, the LIESST effect is weaker than in the case of **3** because ca. 60−80% of the Fe^{II} sites are in the HS state at 5 K. Subsequent irradiation with red laser light (λ_{max} = 806 nm) at 5 K induced a decrease of the $\chi_M T$ value down to 1.7 cm^3 K mol^{-1}, a value much smaller than the initial one, 2.6 cm^3 K mol^{-1} (before irradiation with green and red light). It is noteworthy that the red light irradiation may induce a HS → LS transition (reverse-LIESST effect) of the Fe^{II} sites of $[Fe^{II}H_3L^{Me}][Fe^{III}L^{Me}](NO_3)_2$ (**4**) which could not be achieved thermally.

In independent experiments, following irradiation of the sample up to saturation either with green or red light, the light was switched off, and then the thermal relaxation process was studied by monitoring the $\chi_M T$ value on warming the sample. Figure 20b shows that the thermal relaxation process was completed at ca. 70 K in both cases (green or red light irradiation). These experiments also suggest that the Fe^{II} sites of $[Fe^{II}H_3L^{Me}][Fe^{III}L^{Me}](NO_3)_2$ (**4**) exhibit LIESST and reverse-LIESST effects but the Fe^{III} sites do not.

Concluding Remarks. A new family of complexes, including an HS-Fe^{II} complex $[Fe^{II}H_3L^{Me}](NO_3)_2{\cdot}1.5H_2O$ (**1**), an SCO Fe^{III} complex $[Fe^{III}L^{Me}]{\cdot}3.5H_2O$ (**2**), an SCO Fe^{II}−Fe^{II} complex $[Fe^{II}H_3L^{Me}][Fe^{II}L^{Me}]NO_3$ (**3**), and an SCO mixed-valence complex $[Fe^{II}H_3L^{Me}][Fe^{III}L^{Me}](NO_3)_2$ (**4**), has been characterized and extensively investigated. The coordination chemistry of iron so far reported reveals that ligands with pyridine and imidazole nitrogen donors yield stable Fe^{II} complex, and ligands with carboximate, oxime, and carboxylate groups exhibit a preference for Fe^{III} centers. Within each oxidation state, the ligands which afford SCO are further limited because the ligand field in an SCO compound should be close to the crossover point of the Tanabe−Sugano diagram. In fact, the ligand environments which induce SCO for Fe^{II} are limited to the N$_6$ donor atom sets of pyridine, triazole, pyrazoyl, tetrazole, and imidazole derivatives,[8,10,11] the N$_4$O$_2$ donor atom set of Schiff bases,[23] and a P$_4$Br donor atom set (bromide anion and hexaphenyl-1,4,7,10-tetraphosphadecane).[24] The ligand environments which induce SCO for Fe^{III} are limited to the N$_4$O$_2$ and S$_6$ sets of donor atoms.[25] Therefore, it should be stressed that the present tripodal ligand containing three imidazole groups provides an N$_6$ donor set able to stabilize a remarkable variety of oxidation and spin states of iron, as described in this study. Among the materials in this family, $[Fe^{II}H_3L^{Me}][Fe^{II}L^{Me}]NO_3$ (**3**) and $[Fe^{II}H_3L^{Me}][Fe^{III}L^{Me}](NO_3)_2$ (**4**) assume a homochiral 2D sheet structure based on imidazole−imidazolate hydrogen bonds between H$_3$L^{Me} and L^{Me}. The degree of deprotonation and the substituent effect of the methyl group at the imidazole moiety allow fine-tuning of the electronic states and SCO behavior of this type of molecular system. The combination of optical, SCO, and mixed-valence properties with chirality of the multidimensional extended structure in this family opens up new prospects for the effective use of SCO materials.

Experimental Section

Materials. All chemicals and solvents were reagent grade and were obtained from Tokyo Kasei Co., Ltd., and Wako Pure

---

(23) (a) Petrouleas, V.; Tuchagues, J.-P. *Chem. Phys. Lett.* **1987**, *137*, 21−25. (b) Rakotonandrasana, A. S.; Boinnard, D.; Petrouleas, V.; Cartier, C.; Verdaguer, M.; Savariault, J.-M.; Tuchagues, J.-P. *Inorg. Chim. Acta* **1991**, *180*, 19−31. (c) Boinnard, D.; Bousseksou, A.; Dworkin, A.; Savariault, J.-M.; Varret, F.; Tuchagues, J.-P. *Inorg. Chem.* **1994**, *33*, 271−281. (d) Bousseksou, A.; Tommasi, L.; Lemercier, G.; Varret, F.; Tuchagues, J.-P. *Chem. Phys. Lett.* **1995**, *243*, 493−499. (e) Bousseksou, A.; Salmon, L.; Varret, F.; Tuchagues, J.-P. *Chem. Phys. Lett.* **1998**, *282*, 209−214. (f) Salmon, L.; Donnadieu, B.; Bousseksou, A.; Tuchagues, J.-P. *C. R. Acad. Sci., Ser. IIc: Chim.* **1999**, 305−309.

(24) (a) Bacci, M.; Midollini, S.; Stoppioni, P.; Sacconi, L. *Inorg. Chem.* **1973**, *12*, 1801. (b) Bacci, M.; Ghilardi, C. A. *Inorg. Chem.* **1974**, *13*, 2398. (c) Bacci, M.; Ghilardi, C. A.; Orlandini, A. *Inorg. Chem.* **1984**, *23*, 2798−2802.

(25) (a) Maeda, Y.; Oshio, H.; Takashima, Y.; Mikuriya, M.; Hidaka, M. *Inorg. Chem.* **1986**, *25*, 2958−2962. (b) Conti, A. J.; Chandha, R. K.; Sena, K. M.; Rheingold, A. L.; Hendrickson, D. N. *Inorg. Chem.* **1993**, *32*, 2670−2680. (c) Patra, A. K.; Olmstead, M. M.; Mascharak, P. K. *Inorg. Chem.* **2002**, *41*, 5403−5409. (d) Tweedle, M. F.; Wilson, L. J. *J. Am. Chem. Soc.* **1976**, *98*, 4824−4834. (e) Matsumoto, N.; Ohta, S.; Yoshimura, C.; Ohyoshi, A.; Kohata, S.; Okawa, H.; Maeda, Y. *J. Chem. Soc., Dalton Trans.* **1985**, 2575−2584. (f) Maeda, Y.; Takashima, Y.; Matsumoto, N.; Ohyoshi, A. *J. Chem. Soc., Dalton Trans.* **1986**, 1115−1123. (g) Sim, P. G.; Sinn, E. *Inorg. Chem.* **1978**, *17*, 1288−1290. (h) Nishida, Y.; Oshio, S.; Kida, S. *Chem. Lett.* **1975**, 79−80.

Chemical Industries, Ltd. They were used for the syntheses without further purification. Reagents used for the physical measurements were of spectroscopic grade.

Tris[2-(((2-methylimidazol-4-yl)methylidene)amino)-ethyl]amine H_3L^{Me}. Tris(2-aminoethyl)amine (0.75 g, 5 mmol) was added to a solution of 2-methyl-4-formylimidazole (1.65 g, 15 mmol) in 20 mL of methanol, and the mixture was stirred at 50 °C for 10 min. The methanolic solution of the tripod-type ligand thus prepared was used without isolation of the ligand for the synthesis of the metal complexes.

$[Fe^{II}H_3L^{Me}](NO_3)_2 \cdot 1.5H_2O$ (1). Method A. To the tripod ligand solution (5 mmol in 10 mL of methanol) was added a solution of $Fe^{II}Cl_2 \cdot 4H_2O$ (1.02 g, 5 mmol) in 20 mL of methanol and then a solution of $NaNO_3$ (1.30 g, 15 mmol) in 20 mL of methanol. The mixture was stirred for 5 min at ambient temperature and then filtered. The filtrate was allowed to stand for several days, during which time yellow crystals precipitated. They were collected by suction filtration, washed with a small volume of methanol, and dried in vacuo. Recrystallization was performed from the methanol solution containing a small amount of HCl. Yield: 0.77 g (24%). Anal. Calcd for $[Fe^{II}H_3L^{Me}](NO_3)_2 \cdot 1.5H_2O$: C 40.07, H 5.28, N 26.70. Found: C 39.91, H 5.40, N 26.49. IR(KBr): $\nu_{C=N}$ 1644 cm^{-1}, ν_{NO3} 1370 cm^{-1}.

Method B. To the tripod ligand solution (5 mmol in 10 mL of methanol) was added a solution of $Fe^{III}(NO_3)_3 \cdot 9H_2O$ (2.13 g, 5 mmol) in 20 mL of methanol. The mixture was stirred for 1 day at 30 °C and then filtered. The filtrate was allowed to stand for several days, during which time red-yellow crystals precipitated. They were collected by suction filtration, washed with a small volume of methanol, and dried in vacuo. Recrystallization was performed from the methanol solution containing a small amount of HCl, during which time yellow crystals precipitated. Yield: 1.33 g (50%).

$[Fe^{III}L^{Me}] \cdot 3.5H_2O$ (2). Method A. Tris(2-aminoethyl)amine (0.73 g, 5 mmol) in 10 mL of methanol was added to a solution of 2-methyl-4-formylimidazole (1.65 g, 15 mmol) in 20 mL of methanol, and the mixture was stirred at 30 °C for 60 min. To the ligand solution was added a solution of anhydrous $Fe^{III}Cl_3$ (0.81 g, 5 mmol) in 10 mL of methanol, and then, 10 mL of water was added to the mixture. An aqueous solution of 1 M KOH (ca. 3 equiv) was finally added to the mixture. The reaction mixture was stirred for several hours at room temperature until the solution became blue. The small amount of red precipitate which formed meanwhile ($[Fe^{II}H_3L^{Me}][Fe^{II}L^{Me}]NO_3$ (**3**)) was filtered off. The filtrate was allowed to stand for several days during which time dark blue crystals were precipitated. They were collected by suction filtration, washed with a small volume of methanol, and dried in vacuo. Yield: 0.5 g. Anal. Calcd for $[Fe^{III}L^{Me}] \cdot 3.5H_2O$: C 46.85, H 6.37, N 26.02. Found: C 46.74, H 6.25, N 25.99. IR(KBr): $\nu_{C=N}$ 1601 cm^{-1}.

Method B. Compound **2** was also obtained by reacting a solution of **1** (5 mmol in 30 mL of methanol) with 3 equiv of 1 M aqueous NaOH solution.

$[Fe^{II}H_3L^{Me}][Fe^{II}L^{Me}]NO_3$ (3). To a warm methanol solution of $[Fe^{II}H_3L^{Me}](NO_3)_2 \cdot 1.5H_2O$ (**1**) (0.27 g, 5 mmol) was added 1 equiv of a 0.1 M aqueous KOH solution. The mixture was warmed on a hot plate, and the color of the solution gradually changed from yellow-orange to dark red, and the compound $[Fe^{II}H_3L^{Me}][Fe^{II}L^{Me}]$-$NO_3$ (**3**) crystallized in several hours. The red-black crystalline precipitate was collected by suction filtration, washed with a small volume of methanol, and dried in vacuo. Yield: 0.13 g (52%). Anal. Calcd for $[Fe^{II}H_3L^{Me}][Fe^{II}L^{Me}]NO_3$: C 49.66, H 5.66, N 28.96. Found: C 49.61, H 5.63, N 29.05. IR(KBr): $\nu_{C=N}$ 1637 cm^{-1}, ν_{NO3} 1385 cm^{-1}.

$[Fe^{II}H_3L^{Me}][Fe^{III}L^{Me}](NO_3)_2$ (4). $[Fe^{II}H_3L^{Me}](NO_3)_2 \cdot 1.5H_2O$ (**1**) (0.31 g, 0.5 mmol) in 10 mL of methanol was added to a solution of $[Fe^{III}L^{Me}] \cdot 3.5H_2O$ (**2**) (0.27 g, 0.5 mmol) in 10 mL of methanol at room temperature. The mixture was allowed to stand for several days at room temperature. The black crystalline precipitate was collected by suction filtration, washed with a small volume of methanol, and dried in vacuo. Yield: 0.105 g (19%). Anal. Calcd for $[Fe^{II}H_3L^{Me}][Fe^{III}L^{Me}](NO_3)_2$: C 46.81, H 5.33, N 28.59. Found: C 46.74, H 5.38, N 28.38%. IR (cm^{-1}): $\nu_{C=N}$ 1634, 1614 cm^{-1}; ν_{NO3} 1334 cm^{-1}.

Physical Measurements. The elemental C, H, and N analyses were carried out by Miss Kikue Nishiyama at the Center for Instrumental Analysis of Kumamoto University. Infrared spectra were recorded on a Perkin-Elmer FT-IR PARAGON 1000 spectrometer using KBr disks at room temperature. The ambient temperature (297 K) magnetic moments of **1** and **2** were measured by the Evans method[26] on a Varian Mercury 300 spectrometer (^1H at 300 MHz). In the coaxial tube configuration, the outer 5 mm tube contained solvent (CD_3OD-2% t*ert*-butyl alcohol) while the inner tube contained a dissolved sample (ca. 0.01 M). The frequency difference between the *tert*-butyl alcohol reference signals was measured. Diamagnetic susceptibility corrections were made by using Pascal's constants. TG and DSC measurements were performed with a Perkin-Elmer TGA 7 and DSC 7, respectively, in which the heating rate is 5 K min^{-1}. Magnetic susceptibilities were measured using an MPMS5 SQUID (Quantum Design) in the 5−350 K temperature range at 1 K min^{-1} sweeping rate under an applied magnetic field of 1 T. The calibration was done with palladium metal. Corrections for diamagnetism were applied using Pascal's constants. For the LIESST and reverse-LIESST experiments, a xenon arc lamp (Hamamatsu L7810) and diode laser (806 nm, ILX Lightwave LDT-5525, LDX-3525) were used as the light sources. For the green light, the interference filter with a central wavelength of 500 nm and fwhm = 80 nm (Edmond Ind. Tech. Spec.) was used. The light was guided via an optical fiber into the SQUID magnetometer. The sample was placed on the edge of the optical fiber. The measurements were performed on a very thin layer of powder sample. The weight was estimated by comparing the thermal spin crossover curve with that for a heavier and accurately weighed sample. The Mössbauer spectra were recorded by using a Wissel 1200 spectrometer and a proportional counter. $^{57}Co(Rh)$, moving in a constant acceleration mode, was used as the radioactive source. The hyperfine parameters were obtained by least-squares fitting to Lorentzian peaks. The isomer shifts are reported relative to metallic iron foil at 293 K. The sample temperature was controlled by a Heli-tran liquid transfer refrigerator (Air Products and Chemicals, Inc.) with an accuracy of ±0.5 K. Cyclic voltammetry measurements were performed using a Fuso HECS 321B potential sweep unit with methanol solutions containing $(n\text{-}C_4H_9)_4NBF_4$ (0.1 M) as a supporting electrolyte at a scan rate of 100 mV s^{-1} (CV). The electrochemical cell was a three-electrode system consisting of a glassy carbon working electrode, a platinum wire auxiliary electrode, and a Ag/Ag^+ (Ag/0.01 M $AgNO_3$) reference electrode. As an external standard, the Fc/Fc^+ (Fc = ferrocene) couple was observed at −0.170 V versus Ag/Ag^+ under the same conditions.

Electronic Absorption Spectra. The electronic absorption spectra were recorded with a Shimadzu UV−vis spectrophotometer UV-2450 at 20 °C. The electronic spectral change was recorded upon the addition of 0.10 M NaOH and HCl aqueous solutions for

---

(26) (a) Deutsch, J. L.; Poling, S. M. *J. Chem. Educ.* **1969**, *46*, 167−168. (b) Schubert, E. M. *J. Chem. Educ.* **1992**, *69*, 62.

the forward and reverse processes, respectively.[27] An aqueous solution of the protonated complex (0.5 mM methanol, 50 mL) was prepared. The spectrum was recorded after every 0.075 mL addition of 0.10 M NaOH solution until 3 equiv of NaOH were added. The time dependence of the spectrum was measured for the mixed solution of **1** and 3 equiv of NaOH at 20 °C. For the reverse process, the electronic spectrum of $[\mathrm{Fe^{III}L^{Me}}]\cdot 3.5\mathrm{H_2O}$ (**2**) (0.5 mM methanol, 50 mL) was measured with the addition of 0.075 mL of 0.10 M HCl solution. The spectra were corrected for the volume variation due to the addition of the NaOH and HCl solutions.

X-ray Data Collection, Reduction, and Structure Determination. The X-ray diffraction data for $[\mathrm{Fe^{III}L^{Me}}]\cdot 3.5\mathrm{H_2O}$ (**2**) were collected using a Rigaku AFC-7R diffractometer at 293 K. The data were corrected for Lorentz, polarization, and absorption effects. The structure was solved by direct methods and expanded using the Fourier technique.[28] Hydrogen atoms were fixed at the calculated positions and refined using a riding model. All calculations were performed using the Crystal Structure crystallographic software package.[29]

The crystal structure of $[\mathrm{Fe^{II}H_3L^{Me}}][\mathrm{Fe^{II}L^{Me}}]\mathrm{NO_3}$ (**3**) was determined at 293, 130, and 90 K. The selected crystal (red parallelepiped, 0.25 × 0.20 × 0.15 mm^3) was mounted on an Oxford-Diffraction Xcalibur diffractometer using graphite monochromated Mo Kα radiation (λ = 0.71073 Å) and equipped with an Oxford Instruments Cryojet cooler device.[30] There were 12 042 reflections collected at 293 K, of which 4955 were independent ($R_{\mathrm{int}} = 0.0493$), 11 499 reflections at 130 K, of which 4735 were independent ($R_{\mathrm{int}} = 0.0452$) and 10 345 reflections at 90 K, of which 4609 were independent ($R_{\mathrm{int}} = 0.0441$). No absorption corrections were applied. The structures were solved by direct methods using SHELXS-97[31] and refined on F^2 by full-matrix least-squares using SHELXL-97[32] with anisotropic displacement parameters for all the non-hydrogen atoms, except for the disordered nitrate anion atoms. The H atoms were introduced into the calculations using the riding model with isotropic thermal parameters 1.1 times higher than those of the atom to which they are bonded. Scattering factors were taken from the literature.[33]

Acknowledgment. This work was supported in part by a Grant-in-Aid for Science Research (14340209) from the Ministry of Education, Science, Sports, and Culture, Japan, and the Fund for Project Research from the Venture Business Laboratory, Graduate School of Okayama University. Y.S. thanks the Japan Society of Promotion for Science for a postdoctoral fellowship.

Supporting Information Available: X-ray crystallographic files in CIF format for compounds **2** and **3**. This material is available free of charge via the Internet at http://pubs.acs.org.

IC034495F

---

(27) (a) Matsumoto, N.; Motoda, Y.; Matsuo, T.; Nakashima, T.; Re, N.; Dahan, F.; Tuchagues, J.-P. *Inorg. Chem.* **1999**, *38*, 1165−1173. (b) Matsumoto, N.; Mizuguchi, Y.; Mago, G.; Eguchi, S.; Miyasaka, H.; Nakashima, T.; Tuchagues, J.-P. *Angew. Chem., Int. Ed. Engl.* **1997**, *36*, 1860−1862.

(28) Beurskens, P. T.; Admiraal, G.; Beurskens, G.; Bosman, W. P.; de Gelder, R.; Israel, R.; Smits, J. M. M. *The DIRDIF-99 program system*; Technical Report of the Crystallography Laboratory; University of Nijmegen: The Netherlands, 1999.

(29) *CrystalStructure 2.00; Crystal Structure Analysis Package*; Rigaku and Molecular Structure Corporation, Tokyo, 2001.

(30) Watkin, D. J.; Prout, C. K.; Carruthers, J. R.; Betteridge, P. W. *CRYSTALS Issue 10*; Chemical Crystallography Laboratory: Oxford, U.K, 1996. *CRYSALIS Version 169*; Oxford-Diffraction, Oxford, 2001.

(31) Sheldrick, G. M. *SHELXS-97. Program for Crystal Structure Solution*; University of Göttingen: Göttingen, Germany, 1990.

(32) Sheldrick, G. M. *SHELXL-97. Program for the refinement of crystal structures from diffraction data*; University of Göttingen: Göttingen, Germany, 1997.

(33) *International Tables for Crystallography*; Kluwer Academic Publishers: Dordrecht, The Netherlands, 1992; Vol. C.